



Investigation of Saharan dust plumes in Western Europe by remote Sensing, in situ measurements, and transport modelling

Hengheng Zhang¹, Gholam Ali Hoshyaripour¹, Heike Vogel^{1*}, Frank Wagner², Thomas Leisner¹, Jochen Förstner², and Harald Saathoff¹

¹Institute of Meteorology and Climate Research, Karlsruhe Institute of Technology, Eggenstein-Leopoldshafen, Karlsruhe, Germany

²Deutscher Wetterdienst (DWD), Frankfurter Str. 135, 63067 Offenbach am Main, Germany

^{3*} Retired

Correspondence: Hengheng Zhang (zhang@riam.kyushu-u.ac.jp) and Harald Saathoff (Harald.Saathoff@kit.edu)

Abstract. The radiative forcing of atmospheric dust remains highly uncertain due to the significant spatial and temporal variability of dust particles, as well as their complex interactions with atmospheric constituents, radiation, and clouds. To investigate Saharan dust plumes in Western Europe, we collected comprehensive datasets from remote sensing observations (lidars & photometers), in-situ measurements (aerosol particle size & number), and model calculations (ICON-ART) for 4 different time periods with strong Saharan dust influence in southwest Germany. We determined Saharan dust properties and transport pattern employing these comprehensive datasets. Comparison between lidar measurements, sun photometer data, and ICON-ART predictions shows a relative good agreement for dust plume arrival times (± 20 min), dust layer heights and structures (± 50 m), backscatter coefficients ($\pm 0.16 \text{ Mm}^{-1} \text{sr}^{-1}$ at 355 nm), aerosol optical depths (± 0.05 at 500 nm), demonstrating the capabilities of ICON-ART in predicting Saharan dust transport. The deviation observed for different meteorological conditions and at different locations are discussed in this paper to substantiate the model validation and to facilitate potential improvement of processes like dust emission, transport, aging, removal, as well as dust properties (size distribution, optics, micro-physics) in transport models like ICON-ART. This study contributes to better understand dust properties in Western Europe and helps to improve model capabilities in predicting Saharan dust plumes as well as their potential impact on clouds and weather.

1 Introduction

The Saharan desert is the largest source of aeolian dust in the world, with annual production rates of about $4 - 7 \times 10^8$ tons/year, which is almost half of all aeolian dust inputs to the oceans (Middleton and Goudie, 2001). Saharan dust is mainly produced by natural processes such as wind storms and doesn't appear to be heavily impacted by human activities (Kandler et al., 2007). Saharan dust has been found to be transported in the free troposphere over long distances reaching e.g. the Amazon basin, middle and north America, Europe (Guerzoni and Chester, 1996), even Japan (Tanaka et al., 2005), and other regions. The Saharan dust impacts ecosystems and human life in the following ways. Firstly, dust impacts ecosystems in various regions like the Atlantic Ocean, the Amazon basin, the southeastern United States, or the Caribbean by providing limiting nutrients such as phosphorus or iron, and in some cases promoting soil development (Molinaroli et al., 1993). Secondly, Saharan dust



has also impact on power supply by changing photovoltaic output. When it comes to Saharan dust outbreaks, the photovoltaic output is reduced not only through a significant increase in aerosol optical thickness, but also through dust deposition on the 25 photovoltaic modules on subsequent days (Conceição et al., 2018; Rieger et al., 2017a). Thirdly, Saharan dust particles can also act as cloud condensation nuclei (CCN) or ice-nucleating particles (INP), influencing cloud formation and thereby altering radiative forcing through aerosol indirect effects (Seifert et al., 2023). Finally, Saharan dust outbreaks has impact on short-range weather forecast errors as current weather prediction models still struggle to reproduce cloudiness and radiative 30 effects during dust events, largely because of missing or simplified representations of aerosol–cloud interactions, especially the indirect effects of dust (Hermes et al., 2024).

Changes in circulation patterns associated with climate change have led to an increase in frequency and intensity of Saharan dust events in the Carpathian Basin (Varga, 2020). The annual number of dust events was 4.2 on average between 1979 and 2010, while in the period of 2011–2018, it has increased to 10.3. And an average of about 33,000 tons of atmospheric dust was transported to Central Europe each year from 2002–2017 (Rostási et al., 2022). The increased frequency and amount of 35 Saharan dust plumes have caused larger uncertainties in global radiative forcing (Saidou Chaibou et al., 2020; Diop et al., 2020; Mallet et al., 2009).

The predictions of Saharan dust plume regarding dust arrival time, dust height and structure, as well as dust impact on clouds, precipitation, and convective systems is meaningful. In past decades, different transport models were developed to simulate the distribution and evolution of aerosol over the globe. For example, the general circulation model the ECHAM-HAMMOZ (Pozzoli et al., 2008a, b), the ECHAM/MESSy Atmospheric Chemistry (EMAC) (Roeckner et al., 2006; Jöckel et al., 2006, 2010), the Whole Atmosphere Community Climate Model (WACCM) (Kunz et al., 2011; Smith et al., 2011), the Weather Research and Forecasting (WRF) model coupled with Chemistry (WRF/Chem) (Chapman et al., 2009), the CONsortium for small-scale MOdeling (COSMO) and its extension on Aerosol and Reactive Trace gases (ART) (Vogel et al., 2014), and its successor the ICOsahedral Nonhydrostatic (ICON) and its extension on Aerosol and Reactive Trace gases (ART) (Rieger et al., 2015; 40 Weimer et al., 2017). A multi-model forecast comparison is now also available by the Sand and Dust Storm Warning Advisory and Assessment System (Benincasa, 2023), a program of the World Meteorological Organization (WMO). The Dust-DN (Dust Doctoral Network) project, an EU-funded initiative under the Horizon Europe program, seeks to advance the scientific understanding of mineral dust processes and improve the predictive capabilities of dust transport models (<https://dust-dn.cyi.ac.cy/>, last access: 26 December 2024).

50 Different dust transport models need to be evaluated against a range of measurement methods, including both remote sensing and in-situ observations. This comparison is essential for validating model performance, assessing the validity of parameterizations used in the models, and improving our understanding of aerosol properties and processes during dust events (Zhang et al., 2022; Hoshayaripour et al., 2019). For example, aerosol lidar is a useful tool to validate Saharan dust model simulations as it can provide high-resolution vertical profiles of dust plumes (Chouza et al., 2016; Zhang et al., 2022). Ground-based lidar 55 networks including the European Aerosol Research Lidar Network (EARLINET) (Mona et al., 2014), the Micro-Pulse Lidar Network (MPLNET) (Misra et al., 2012), and the Asian Dust and Aerosol Lidar Observation Network (AD-Net) (Sugimoto et al., 2016) have conducted long-term dust observation in last decades to investigate dust transport and optical proprieties.



Also the sun photometers deployed by the Aerosol Robotic Network (AERONET) (Kim et al., 2011) provides rich information on column integrated dust optical parameters (e.g. Aerosol optical depth (AOD), Ångström Exponent (AE), single scattering albedo (SSA)). Finally, satellite data can also be used to study Saharan dust properties and validate Saharan dust transport model. For example, the MODIS instrument aboard the Terra & Aqua satellites can provide column integrated aerosol optical properties (Merdji et al., 2023; Barnaba and Gobbi, 2004) and the Cloud-Aerosol Lidar with Orthogonal Polarization (CALIOP) aboard of the CALIPSO satellite can provide vertical profiles of aerosol information (Hoshyaripour et al., 2019; Liu et al., 2008). The valuable satellite data provided by these active or passive remote sensing sensors aboard different satellites help to understand the dust properties over the globe (Song et al., 2022; Wu et al., 2020).

Southwest Germany provides an excellent location for investigating Saharan dust plumes. Firstly, this region is frequently affected by long-range transported Saharan dust events, especially during spring and summer seasons (Ansmann et al., 2003; Gasteiger et al., 2011). Second, the typical transport time for dust particles—ranging from 2 to 5 days—makes it ideal for examining long-range dust transport and its interactions with local atmospheric conditions (Ansmann et al., 2003). Additionally, the region's diverse meteorological patterns, including extreme weather events such as storms and prolonged dry periods, play a significant role in dust movement and deposition, offering a wide range of scenarios for analysis (Kunz et al., 2022a). These factors make southwest Germany a key site for validating global transport models, with insights gained here being broadly applicable to other regions with similar characteristics.

Zhang et al. (2022) investigated the properties and transport of Saharan dust during the period from April 7 to 9, 2018, through a synergistic approach combining modeling and observational data. They demonstrated that a novel method for retrieving the lidar ratio from scanning aerosol lidar measurements could be effectively applied to this dust plume, yielding optical parameters (e.g., lidar ratio and particle depolarization ratio) consistent with values reported in the literature. Their study also showed that the modeled backscatter coefficients agreed well with lidar observations when non-spherical particles were assumed, with a slope of 0.9 ± 0.1 ($R^2 = 0.68$). In contrast, assuming spherical particles led to a significant overestimation, with a slope of 2.3 ± 0.3 ($R^2 = 0.74$). In the present study, we utilize a more comprehensive dataset to investigate the evolution and optical properties of dust in southwest Germany, extending the analysis to a broader set of dust events and characteristics. A scanning aerosol lidar system, a sun photometer, different ground-level in situ aerosol characterisation instruments (e.g. Optical Particle counter (OPC)), the MODIS satellite (Remer et al., 2005), and a Saharan dust transport model, ICON-ART model Zängl et al. (2015), were employed in 4 Saharan dust cases to investigate these dust events employing different retrieval methods. The MODIS satellite provides spatial distribution of AOD, aiding in the study of Saharan dust transport, while ground-based measurements offer continuous data for southwest Germany. The major objective was to assess the performance of dust prediction for ICON-ART, to identify model improvements, and to better understand dust properties during these dust events benefiting from the advanced instruments.

This paper is organised as follows. Section 2 describes the remote sensing and in situ methods as well as the model simulations. Details of the dust observations and dust properties are discussed in section 3 including a comparison of the different remote sensing and in situ methods as well as how they compare to the model predictions. In the final section, we provide some conclusions.



2 Method

Four Saharan dust events were investigated combining remote sensing, ground-level in situ measurements, and a transport model over western Europe. The four selected cases were chosen to address different scientific objectives and to sample a broad range of aerosol and cloud conditions. Case 1 is designed to evaluate the added value of scanning lidar relative to vertically pointing lidar observations, with a particular focus on additional information provided by scanning measurements that cannot be captured by single-column observations. Case 2 corresponds to the longest cloud-free Saharan dust episode, lasting approximately six days, and serves as a reference case for examining the temporal evolution and vertical structure of dust plumes under clear-sky conditions. Case 3 documents the interaction between Saharan dust and clouds, allowing an investigation of dust–cloud coupling processes and their influence on observed vertical structures. Case 4 represents the most intense dust outbreak, with aerosol optical depth (AOD) approaching 2, and is used to assess the vertical distribution and optical characteristics of extremely dense dust layers. Together, these cases provide a comprehensive framework for evaluating lidar observation strategies and for characterizing Saharan dust under diverse atmospheric conditions. A scanning aerosol lidar (Zhang et al., 2022) provided spatial-temporal distributions of Saharan dust plumes and optical properties of dust particles. Also, a sun photometer (Giles et al., 2019) provided wavelength-dependent aerosol optical depth (AOD), Angstrom exponent (AE), and under clear sky conditions the aerosol size distributions (ASD), and single scattering albedo (SSA). Besides, ground-level in situ aerosol characterisation instruments (e.g. OPC, APS, SMPS, and CPC) provided aerosol number concentration and mass concentration as well as aerosol size distribution. Finally, these observational data were compared with predictions from the online coupled model system ICON-ART (Rieger et al., 2015). The model system is running in operational mode by Deutscher Wetterdienst (DWD). The main methods used to characterize the four different Saharan dust events are summarized in table 1.

Table 1. List of main methods used for 4 Saharan dust cases (SPH^a: Sun photometer; KIT-CN^b: KIT campus north). *Please note that the dust particles didn't reach ground level during events 1 & 4 so that no in situ measurements could be conducted.

ID	Date	Observation site	lidar	OPC	APS	SPH ^a	MODIS	ICON-ART
1	April 7 th -9 th , 2018	KIT-CN ^b , (8.4298° E, 49.0953° N)	X			X	X	X
2	February 22 th - 27 th , 2021	KIT-CN, (8.4298° E, 49.0953° N)	X	X	X	X	X	X
3	June 19 th -20 th , 2021	Rottenburg, (8.95452° E, 48.4892° N)	X	X	X	X	X	X
4	March 16 th -22 th , 2022	KIT-CN, (8.4298° E, 49.0953° N)	X			X	X	X



2.1 Remote sensing methods

A scanning aerosol lidar called Karlsruhe scanning aerosol lidar (KASCAL (LR111-ESS-D200, Raymetrics Inc.)) was deployed at the campus north of the Karlsruhe Institute of Technology (8.4298° E, 49.0953° N, 119 m above sea level) for dust events occurred in April 2018, February 2021, and March 2022 and was deployed in Rottenburg am Neckar (8.95452° E, 48.4892° N, 339 m above sea level) for dust events occurred on June 2021 (Kunz et al., 2022b). The KASCAL lidar system is a mobile scanning system with an emission wavelength of 355 nm. The laser head, 200 mm telescope, and lidar signal detection units are mounted on a rotating platform. The overlap range of the lidar system is 255 m and the overlap correction for the KASCAL lidar has been done with horizontal measurements assuming horizontal homogeneous conditions. This KASCAL lidar works automatically, time-controlled, and continuously via a software developed by Raymetrics Inc. (Avdikos, 2015). For the data analysis and calibration of the system, we followed the quality standards of the European Aerosol Research Lidar Network (EARLINET) (Freudenthaler, 2016; Zhang et al., 2022).

The sun photometer (CE-318, CIMEL, Holben et al. (1998)) which measures solar radiance at nine different wavelengths ranging from 339 nm to 1638 nm was also deployed in these four Saharan dust events. The sun photometer data enables calculation of AOD at specific wavelengths. Additionally, the data can be used to determine other important aerosol parameters such as SSA, AE, ASD, and complex refractive index (CRI) (Vermeulen et al., 2000; Sinyuk et al., 2020; Dubovik and King, 2000). SSA measures the ratio of scattering coefficient to extinction coefficient, which is inversely proportional to the aerosol absorption ability. AE describes the wavelength dependency of AOD, which is influenced by particle size. Smaller particles exhibit a stronger wavelength dependency, resulting in a higher AE value. Additionally, clear sky measurements from the sun photometer can be used to derive ASD (between 0.05 – 15 μm), complex refractive index (between 1.33 – 1.6 and 0.0005i – 0.5i), and other parameters (Dubovik and King, 2000; Müller et al., 2010). The sun photometer is part of the Aerosol Robotic Network (AERONET) and level 2.0 data was utilized in this study (Giles et al., 2019).

The Moderate Resolution Imaging Spectroradiometer (MODIS) is an imaging sensor onboard the NASA Terra and Aqua satellites, launched in 2000 and 2002, respectively (Remer et al., 2005). It provides continuous global observations with a wide range of products, including atmospheric, land, and ocean data, at spatial resolutions ranging from 250 m to 1 km. MODIS is widely used for studying aerosol properties, including Aerosol Optical Depth (AOD), which is crucial for monitoring dust transport, climate change, and air quality. The data is available from the NASA LAADS DAAC and has been a key resource in atmospheric and environmental research (Justice et al., 2002; Salomonson et al., 1989).

140 2.2 Ground-level in situ instruments

The ground-level in situ instruments were deployed in a mobile container for the field campaign at Rottenburg am Neckar and were installed in the laboratory of building 322 on campus north of the KIT near the village of Eggebstein-Leopoldshafen. Aerosol particle size distributions were determined using scanning mobility particle sizer (SMPS; DMA: TSI 3080, CPC 3022A, TSI Inc., 14-760 nm), aerodynamic particle sizer (APS; TSI 3321, TSI Inc, 0.5 - 20 μm), and optical particle counter (OPC; Fidas200, Palas, GmbH, 0.18 - 18 μm). Additionally, two condensation particle counters (CPC3776, 3025, TSI Inc.)



counted particle numbers (>2.5 nm) with a time resolution of 1 second. These instruments operated with a flow rate of 5 L/min and a time resolution of 1-5 minutes during Saharan dust events 2 and 3. Additionally, two condensation particle counters (CPC3776, 3025, TSI Inc.) counted particle numbers with a time resolution of 1 second. Meteorological parameters were measured with a compact sensor (WS7000, Luff) (Jiang et al., 2025).

150 2.3 ICON-ART

To predict the transport and distribution of dust in these four Saharan dust events, the ICON-ART model system was used, which is an online-coupled model that integrates weather and climate modeling with the life cycle and feedback of aerosols and trace gases. ICON is a comprehensive model that solves the full three-dimensional non-hydrostatic and compressible Navier-Stokes equations on an icosahedral grid (Zängl et al., 2015), while the ART module extends the model to include 155 aerosols and trace gases. In ART, mineral dust is represented by three lognormal modes, with mass median diameters of 1.5, 6.7, and 14.2 μm , and standard deviations of 1.7, 1.6, and 1.5, respectively. The dust emission scheme is based on (Vogel et al., 2006) and (Rieger et al., 2017b), which consider soil properties, soil dispersion state, and soil type heterogeneity. The model accounts for dust removal processes such as sedimentation, dry, and wet deposition. The simulations were conducted on a global domain with a regional nest over North Africa and Europe, using horizontal resolutions of 40 and 20 km, respectively. 160 The vertical resolution ranges from tens of meters to several kilometers from low to high altitudes with total of 65 layers, with a resolution of 200 to 400 m in the altitude range of 2-6 km, where dust layers from long-range transport are often present.

3 Results and Discussion

3.1 Case 1

The properties and transport of Saharan dust from April 7 to 9, 2018, in case 1 have already been described by Zhang et al. 165 (2022). They demonstrated that a novel method for retrieving the lidar ratio from scanning aerosol lidar data could be applied to this dust plume to determine optical parameters (e.g., lidar ratio and particle depolarization ratio) consistent with values reported in the literature.

3.2 Case 2

Saharan dust case 2 was characterized in February 2021 at the KIT campus north near the city of Karlsruhe by combining 170 remote sensing, ground in situ aerosol characterization instruments, and ICON-ART simulations. For these measurements during February 2021, actually three different dust plumes were observed. In this section, we will focus on the period with the longest duration of nearly 5 days from 22nd to 26th, of February 2021. This period was almost free of clouds. Figure S2 displays the horizontal distributions of daily averaged aerosol optical depth (AOD) from MODIS satellite measurements with a spatial resolution of $0.4^\circ \times 0.4^\circ$, for the period from February 22 to 26, 2021. The data reveal that during this period, Saharan 175 dust originating from North Africa was transported to Karlsruhe, Germany, showing distinct signatures of dust plumes in the

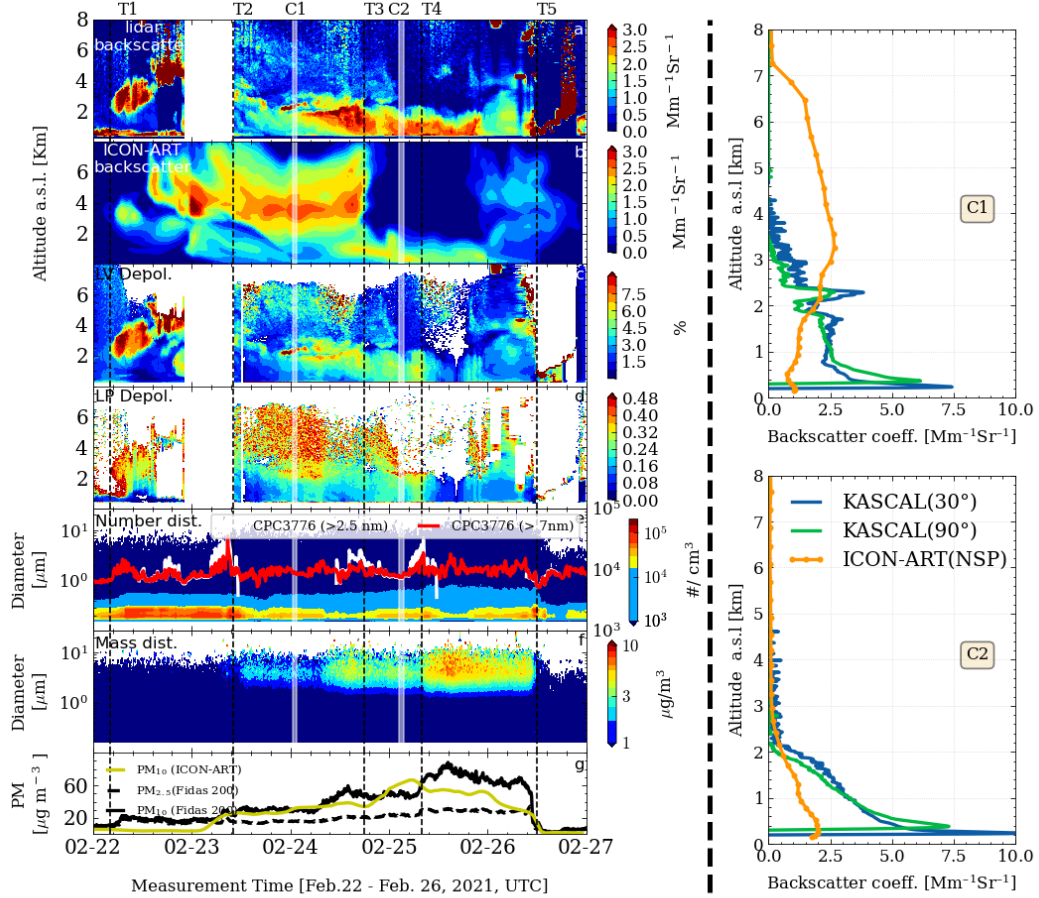


Figure 1. Time series of backscatter coefficients from KASCAL measurements (a), predicted backscatter coefficients by ICON-ART (b), Linear Volume Depolarization Ratio (LVDR) (c) Linear Particle Depolarization Ratio (LPDR) (d) from KASCAL measurements, particle number size distribution from Fidas 200 and particle number concentration from two CPCs (e), particle mass size distribution from Fidas 200 (f) and particulate matter concentrations (PM₁₀ & PM_{2.5}) from the Fidas 200 and the lowest model level (150 m) of the ICON-ART simulation (g) from February 22th to 26th, 2021 for case 2. Please note that the model data shown only includes the Saharan dust while the lidar data shows also other aerosol particles and clouds. The profiles of backscatter coefficients measured by the lidar and predicted by ICON-ART model for case 1 (Averaged profiles from 00:30 to 1:30 for lidar measurement and profile at 01:00 for ICON-ART prediction on 24th, February 2021) and for a selected time C2 (Averaged profiles from 02:30 to 03:30 for lidar measurement and profile at 03:00 for ICON-ART prediction on 25th, February 2021) are shown on the right side of this figure. The vertical dashed lines in the contour plots indicate dust arrival (T1), dust touched to the ground (T2), an increase of PM concentration at ground level (T3 & T4) and a low-level cloud appeared (T5). C1 and C2 represent time periods used for a more detailed data analysis as shown in the right side of this figure.



atmosphere. Figure 1 shows the time series of backscatter coefficients from KASCAL measurements, ICON-ART predicted backscatter coefficients, Linear Volume Depolarization Ratio (LVDR) and Linear Particle Depolarization Ratio (LPDR) from KASCAL measurements, particle number size distributions and particle number concentration from two CPCs, particle mass size distributions and particle matter concentrations from OPC (Fidas200) measurements from 22nd to 26th, February 2021.

180 The KASCAL was operated at two observation angles similar as for case 1 (Zhang et al., 2022) but the lidar data shown in this figure is averaged for each observation angle with an integration time of 300 s. The missing lidar data from 22:15 on 22nd, February to 10:25 on 23rd, February 2021 was due to a technical problems (loss of laser cooling). As can be seen from this figure, the dust arrived at the observation site at 04:00 on 22nd, February 2021 (dashed line T1) and lasted for about 5 days. Initially, the dust plume had a maximum backscatter at around 2.0 km altitude, and then the Saharan dust plume started sinking

185 and reached ground level at 10:00 on 23rd, February 2021 (dashed line T2), and these ground level particles were characterized by an in situ aerosol sizer (Fidas200). Subsequently, the ground level aerosol concentration increased stepwise as can be seen from the mass size distributions (Figure 1f) and particle mass concentrations (Figure 1g) from 12:00 of 24th, February 2021 to 12:00 of 26th, February 2021. However, the increase in particle number concentration is not obvious in Figure 1e, because the aerosol number concentration is dominated by smaller particles. Finally, a sharp decrease of ground level aerosol dust particles

190 and dust concentration at high altitudes can be seen from both, ground level in situ and lidar measurements at 12:00 on 26th, February 2021 (dashed line T5) due to increasing wind speeds advecting clean air masses.

The evolution of the dust plume over Karlsruhe for dust case 2 predicted by the ICON-ART model is shown in Figure 1b. According to the model simulation, the dust plume arrived in Karlsruhe at 04:00 on 22nd, February 2021, and lasted for about five days. Initially, the ICON-ART predicted dust backscatter ranged between 1.0 and 8.0 km. Subsequently, the higher-

195 altitude dust plume disappeared at 18:00 on 24th, February 2021 and the main dust layer reached ground level. The time series of particulate mass concentrations (PM₁₀) from Fidas measurements and dust mass concentration from the ICON-ART simulation, shown in Figure 1g, reveal a good correlation of PM₁₀ between Fidas 200 measurement and ICON-ART prediction, with a slope of 0.754 ± 0.041 and a Pearson correlation coefficient of 0.862, indicating the a relative good performance of the ICON-ART prediction. The dust layer heights predicted by ICON-ART did not agree well with lidar measurements in terms

200 of dust layer height and structure before 18:00 on 24th, February 2021 while it shows consistency after this time. The dust layer heights and their peak heights for both lidar measurement and ICON-ART prediction are shown in Figure 10b. The dust peak heights are not shown after 18:00 on 24th, February 2021 for lidar measurement due to the influence of boundary layer aerosol loading during this time and boundary layer aerosol having maximum values near ground level. The vertical profiles of backscatter coefficients from lidar measurements and ICON-ART calculations are shown at the right of Figure 1 for two

205 selected periods indicated as C1 and C2 in Figure 1. For case C1, the backscatter coefficients are given for lidar measurements from 00:30 to 01:30 and ICON-ART calculations for 01:00 on 24th, February and for case C2, the backscatter coefficients are given as average of lidar measurements between 02:30 to 03:30 and ICON-ART calculations for 03:00 on 25th, February 2021. As can be seen in the vertical profiles for the C2 period, the boundary layer aerosol and dust particles are mixed below 2.0 km and this mixing requires additional analysis to determine dust peak heights from lidar measurements. In addition, the vertical

210 profiles of the backscatter coefficients for period C1 show inconsistencies for dust layer heights and backscatter coefficients



while profiles in case C2 show consistencies in dust layer height but inconsistencies in backscatter coefficients. As discussed for Saharan dust case 1, the predicted backscatter coefficients can agree well with values retrieved from lidar measurements if non-spherical particles are assumed (Zhang et al., 2022). However, during period C2 of Saharan dust case 2, the ICON-ART predicted backscatter coefficients for non-spherical particles were systematically lower than those from lidar retrievals. The 215 main reason for this difference to the backscatter coefficients retrieved from lidar measurements is the contribution of non-dust particles to the total backscatter coefficient in this mixing layer.

Tesche et al. (2009) proposed a method to separate the total backscatter coefficient into a dust part and a non-dust part using the following equation:

$$\beta_{\lambda,d} = \beta_{\lambda,p} \frac{(\delta_{\lambda,p} - \delta_{\lambda,nd})(1 + \delta_{\lambda,d})}{(\delta_{\lambda,d} - \delta_{\lambda,nd})(1 + \delta_{\lambda,p})} \quad (1)$$

220 Where $\beta_{\lambda,d}$ is the pure dust backscatter coefficient, $\beta_{\lambda,p}$ is the total particle backscatter coefficient, $\delta_{\lambda,p}$ is the total particle depolarization ratio, $\delta_{\lambda,nd}$ is the particle depolarization ratio of non-dust particles, $\delta_{\lambda,d}$ is the particle depolarization ratio of the pure dust plume. In this equation, $\beta_{\lambda,p}$ and $\delta_{\lambda,p}$ can be retrieved from lidar measurement. The particle depolarization ratio of pure dust plume, $\delta_{\lambda,d}$, is estimated from the high-altitude dust layer which is not mixed with non-dust particles and the particle depolarization ratio of non-dust particles, $\delta_{\lambda,nd}$, is the average value of particle depolarization measured on 1st, March 2021 225 when there was no dust layer over Karlsruhe. For this Saharan dust case, a value of 0.3 for $\delta_{\lambda,d}$ and a value of 0.046 for $\delta_{\lambda,nd}$ were used.

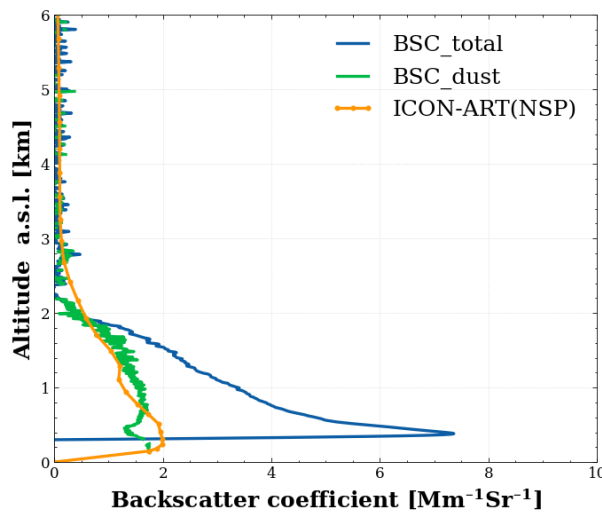


Figure 2. Vertical profile of total backscatter coefficients and dust backscatter coefficients from KASCAL and the predicted backscatter coefficient for non-spherical (NSP) from ICON-ART for period C2 of case 2 (Averaged profiles from 02:30 to 03:30 for lidar measurement and profile at 03:00 for ICON-ART prediction on 25th, February 2021) as indicated in Figure 1.

Figure 2 shows vertical profiles of total backscatter coefficients and pure dust backscatter coefficients from KASCAL measurement and ICON-ART predicted backscatter coefficients for non-spherical particles. This figure shows that backscatter

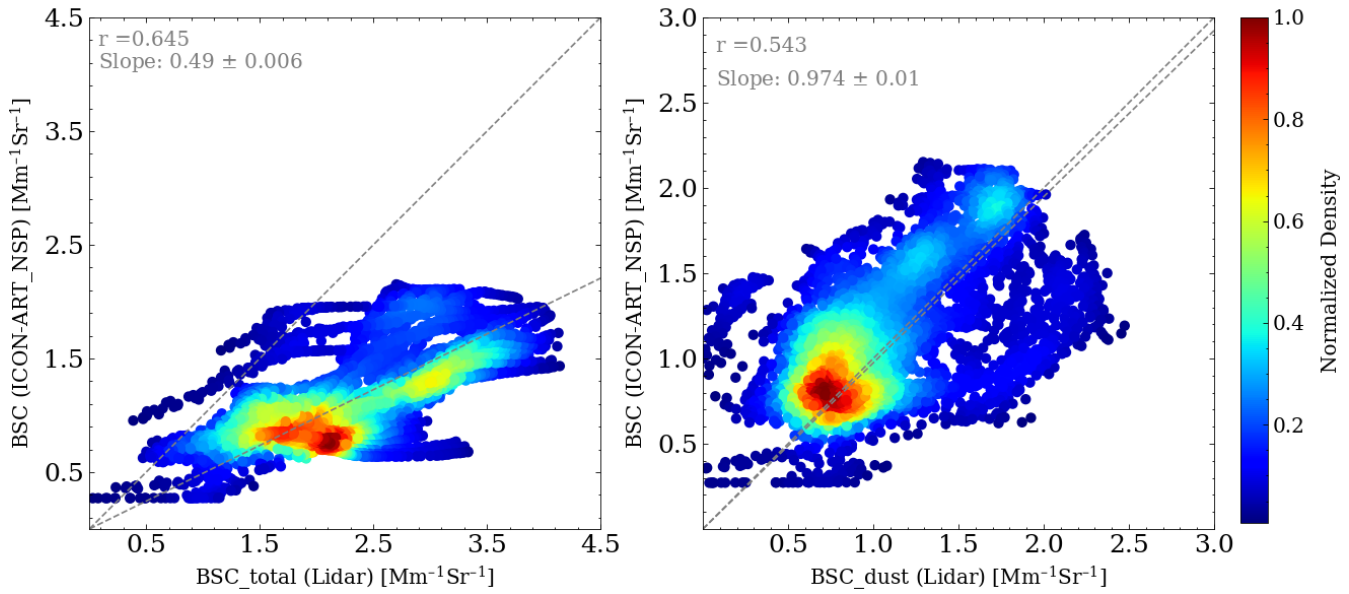


Figure 3. Correlation of backscatter coefficients predicted by ICON-ART for non-spherical (NSP) particles and those retrieved from KASCAL for both total aerosol particles (left) and dust particles only (right) (from 20:00 on 24th to 12:00 to 26th, February 2021 for Case 2).

coefficients predicted by ICON-ART for non-spherical particles are smaller than the total backscatter coefficients measured by KASCAL by a factor of 2.12 ± 0.66 while it agrees well with the pure dust backscatter coefficient by a factor of 1.06 ± 0.22 .
 230 Figure 3 shows the correlation of the backscatter coefficient predicted by ICON-ART for non-spherical particles and those retrieved from KASCAL measurements for both total aerosol particles (left) and dust particles only (right). This correlation only shows the data from 20:00 on 24th to 12:00 on 26th, February 2021 as the dust layer heights are inconsistent between lidar and ICON-ART model before this time. The backscatter coefficients predicted by ICON-ART for dust are systematically lower
 235 than the total backscatter coefficient retrieved from lidar data by a factor of 1.94 ± 0.65 . However, the pure dust backscatter coefficients retrieved from KASCAL agrees well with the backscatter coefficients predicted by ICON-ART for non-spherical particles with the a slop of 0.974 ± 0.01 and a Pearson correlation coefficient of 0.543 as shown in Figure 3. From these comparisons, we can see that the signal from non-dust aerosol particles can successfully be separated from total backscatter coefficients, allowing for a comparison between lidar measurements and ICON-ART simulations for the Saharan dust also
 240 at lower altitudes. The contribution of non-dust aerosol particles can also be seen from comparison of AOD values from sun photometer measurements with ICON-ART results (cf. Figure 5).

Sun photometer data from the Karlsruhe AERONET station were also used to investigate this Saharan dust case. Figure 4 shows the time series of AOD (a), AE (b), SSA (c) measured by the sun photometer for different wavelengths as well as
 245 column-averaged aerosol volume size distributions retrieved from the sun photometer (d) and aerosol mass size distributions

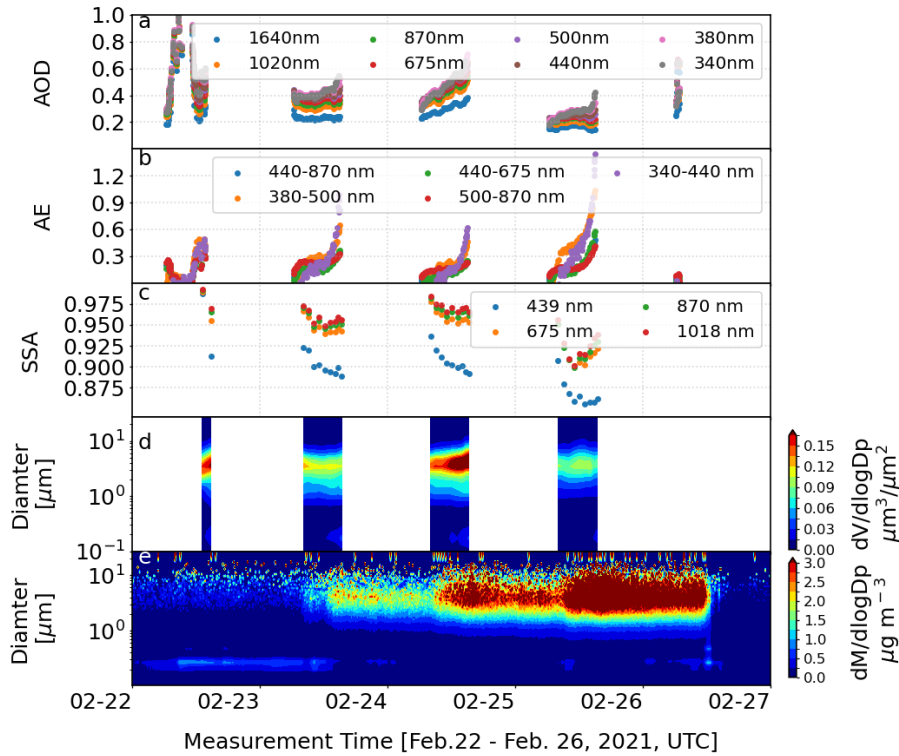


Figure 4. Time series of Aeosol Optical Depth (AOD) (a), Ångström Exponent (AE) (b), Single Scattering Albedo (SSA) (c) at different wavelengths, and column-averaged aerosol volume size distribution (d) measured and retrieved from sun photometer (AERONET, Karlsruhe station) as well as particle mass size distributions (e) measured by Fidas 200 from February 22th to 26th, 2021 for case 2.

measured by Fidas200 at ground level (e). From this figure, we can see a relatively small trend of AOD for different wavelengths caused by large Saharan dust particles over Karlsruhe. These large particles have only very little wavelength dependence in light scattering, thus causing a low value of AE which is below 0.3 most of the time. In addition, the AOD at the wavelength of 340 nm increased from 0.41 at 07:22 of 23rd, February to 0.66 at 15:57 on 24th, February 2021 and then decreased to 0.42 at 16:00 on 25th, February 2021. The SSA shown in panel (c) of this figure indicates that the SSA is wavelength dependent and has the lowest value at a wavelength of 439 nm. This phenomenon is due to the strong absorption of Saharan dust at short wavelengths and this strong absorption caused a low value of SSA. The column-averaged aerosol volume size distribution retrieved from sun photometer and mass size distributions measured by Fidas200 shown in panel (d) and panel (e) show relatively large particles ($d_p > 1 \mu\text{m}$) dominating during this Saharan dust period as expected. In addition, the column-averaged volume size distribution retrieved from sun photometer and the mass size distributions from Fidas200 do not show a similar trend. The volume size distribution retrieved from sun photometer has the highest concentration on 24th, February 2021 while the mass size distribution measured by Fidas200 has the highest concentration on 25th, February 2021. The reason for this inconsistency



can be explained as follow: (1) The sun photometer measures the column integral aerosol from ground level to the tropopause while the Fidas200 measured ground level aerosols. (2) the Saharan dust has the strongest intensity on 24th, February 2021 (as can be seen from AOD value at panel(a)) but most dust particles are aloft (can be seen from lidar measurement shown in the 1a) which cannot be measured by Fidas200 but can be measured by sun photometer. However, on 25th, February, most of the dust particles were sunken to the ground level (as can also be seen from lidar measurement shown in Figure 1a) which were measured by Fidas200. In addition, as the dust plume mass loading on 25th, February 2021 is weaker than that on 24th, February 2021, the column-averaged volume size distribution retrieved by sun photometer for the column aveage is lower on 25th, February 2021.

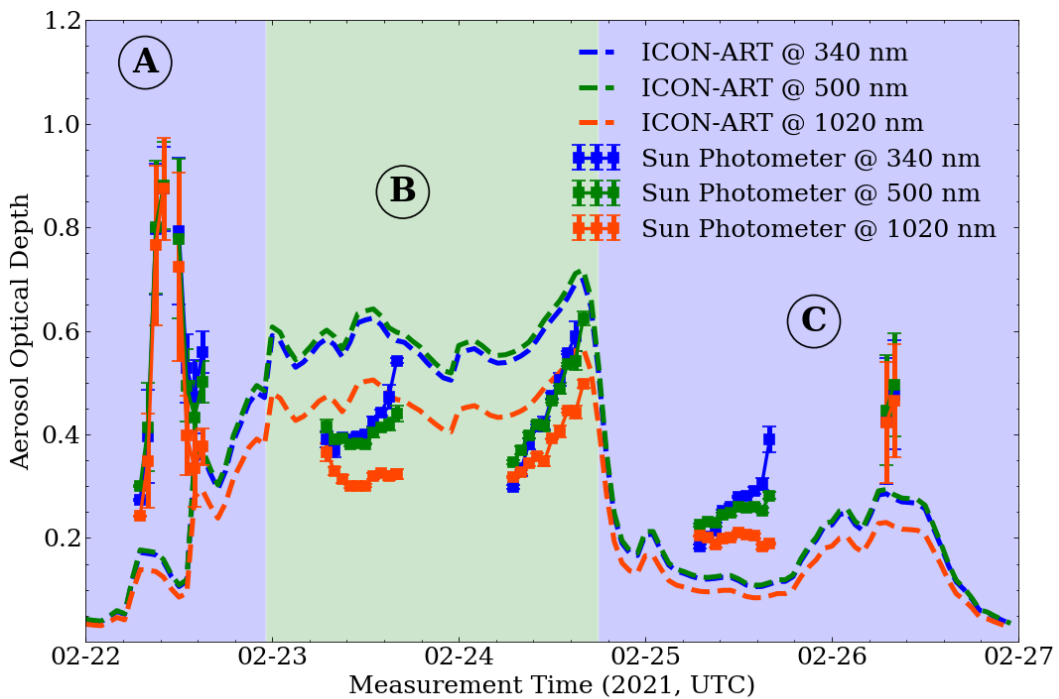


Figure 5. Case 2 time series of AODs at three wavelengths from the sun photometer and ICON-ART model simulations from 22nd, February 2022 to 26th, February 2021 for 1-hour temporal resolution.

265

The time series of AODs at three wavelengths from sun photometer measurements and ICON-ART model simulations from 22nd, February 2022 to 26th, February 2021 are shown in Figure 5. This time series was divided into three periods (A, B, C) as shown in figure 5. This division is based on the relationship of AOD from model simulations and sun photometer data. This figure shows that the AOD measured by the sun photometer is systematically larger than that predicted from ICON-ART by a factor of 2.78 ± 1.60 mainly due to the contribution of non-dust particles as evident for the periods A and C. However, during period B, the AOD from ICON-ART is larger than that measured by the sun photometer by a factor of 1.41 ± 0.18 . The reasons for this discrepancy can be explained as following according to the synoptics of this event. During Period A



(22nd–23rd, February), a strong dust surge associated with a cold front and warm conveyor belt transport led to a rapid AOD increase. ICON-ART underestimates the AOD peak observed by the sun photometer, particularly at 340 nm, suggesting lower simulated dust loading during the initial uplift and long-range transport phase. In Period B (23rd–25th, February), continued dust advection into Central Europe under a stationary Omega block resulted in sustained elevated AOD levels. ICON-ART overestimates AOD across all wavelengths during this period, indicating differences in vertical mixing and removal processes in the model compared to observations under dry, clear-sky conditions. By Period C (25th–27th February), the dust event gradually subsided. Model and observational AOD values show better agreement, though ICON-ART slightly overestimates AOD during some peak periods. Overall, ICON-ART reproduces the general temporal evolution of the dust event but shows discrepancies in magnitude during initial transport and removal phases.

3.3 Case 3

The Saharan dust case 3 was characterized during the Swabian MOSES campaign from June to August 2021 near the city of Rottenburg in western Germany (Kunz et al., 2022b). During this field campaign, several intensive observation periods (IOPs) were conducted and this Saharan dust case was measured during IOP4. Figure S3 presents the horizontal distribution of daily averaged aerosol optical depth (AOD) derived from MODIS satellite observations at a spatial resolution of $0.4^\circ \times 0.4^\circ$, for the period of June 19–20, 2021 (Case 2). During this time, Saharan dust originating from North Africa was transported toward Rottenburg, Germany. Figure 6 shows the time series of range corrected lidar signals (RCS) for the cross-polarized channel and LVDR from KASCAL measurements. The backscatter coefficient and particle depolarizations are not shown in this figure as the retrievals of the backscatter coefficients by the Klett-Fernald method were largely affected by the presence of clouds and this effect would bring large uncertainties in calculating the backscatter coefficients and LPDR. Figure 6 also shows the time series of ICON-ART predicted backscatter coefficients for NSP particles, the particle number and mass size distribution and particulate matter concentrations from OPC, and meteorological parameters from 19th to 20th, June 2021. The KASCAL conducted zenith scans from 90° to 5° elevation angle with the step of 5° at two azimuth angles. The lidar measurements shown in this figure are based only on the vertical profiles extracted from for each scanning plane. As can be seen from this figure, this dust plume arrived in Rottenburg at 11:00 on 19th, June 2021 (dashed line T1) and lasted for nearly 2 days. Initially, the dust layer showed a maximum in volume depolarization ratio at an altitude of 4.0 km which subsequently sunk to an altitude of 2.0 km. At 22:00 on 19th, June 2021, another dust layer with an initial altitude between 2.0 km to 4.0 km arrived at the observation station then subsequently touched ground level at 00:30 on 20th, June 2021 (dashed line T2). Those particles reaching ground level were characterized by the OPC Fidas200 showing an increase in aerosol concentrations until 03:30 (dashed line T3) on 20th, June 2021. At 03:00 on 20th, June 2021, drizzle occurred as shown in panel (g) of this figure and washed the particles out. This caused a decrease of aerosol concentrations measured at ground level. At 11:30 on 20th, June 2021 (dashed line T4), the aerosol particles reached ground level again and caused an increase of aerosol concentrations at ground level from 11:30 on 20th, June 2021 to 19:00 on 20th, June 2021 (dashed line T5). Finally, a moderate rain occurred at around 17:00 on 20th, June 2021 causing a sharp decrease of aerosol particles (T5) due to wet removal.

The evolution of the dust plume over Rottenburg for dust case 3 predicted by the ICON-ART model is shown in Figure 6 c.

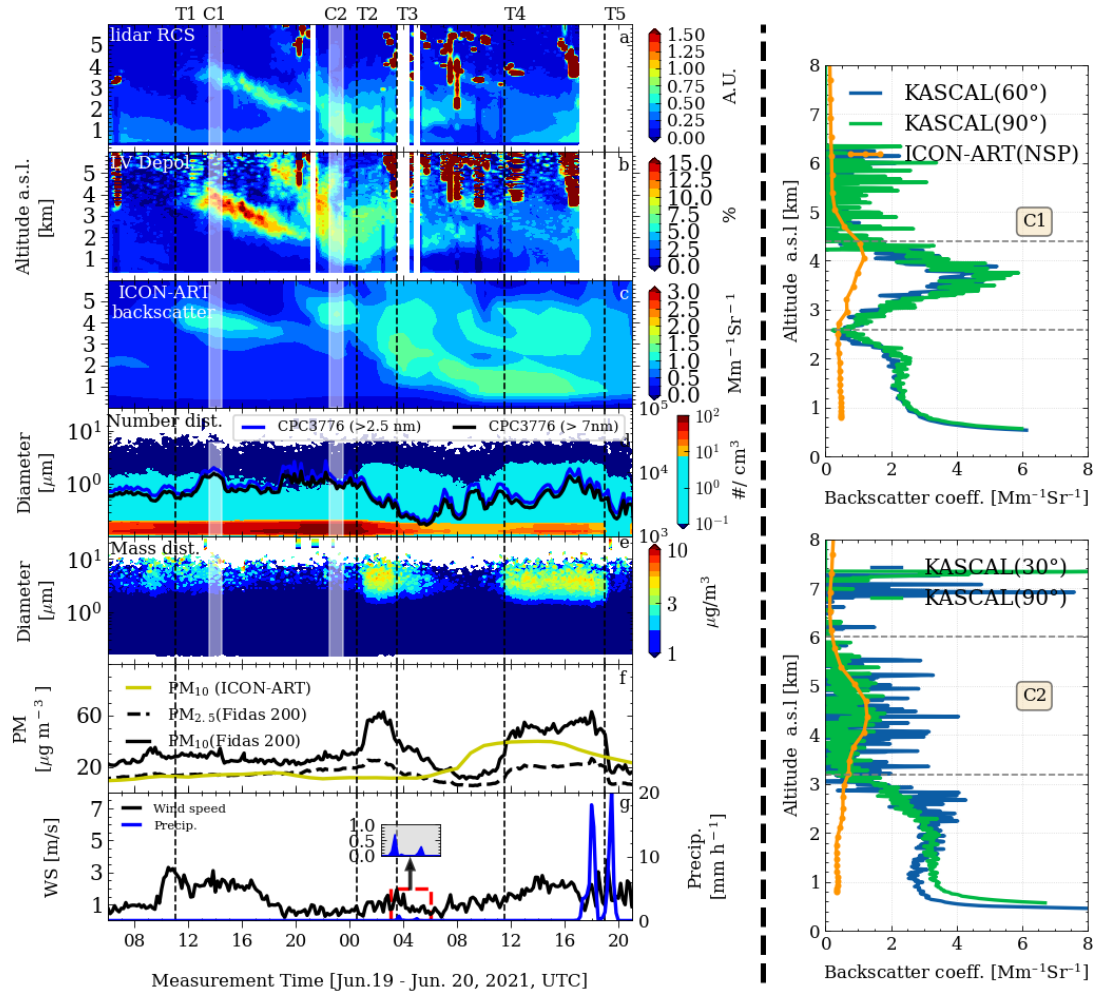


Figure 6. Time series of range corrected lidar signal for the cross-polarized channel (a), and Linear Volume Depolarization Ratio (LVDR) from KASCAL measurements (b), backscatter coefficients predicted by ICON-ART for non-spherical (NSP) particles (c), particle number size distributions from Fidas 200 and particle number concentration from two CPCs (d), particle mass size distributions from Fidas 200 (e) and particulate matter concentrations (PM_{10}) from the Fidas 200 and the lowest model level (150 m) of the ICON-ART simulation (f), and ground level meteorological parameters (e.g. wind, precipitation, WS700) (g) from June 19th to 20th, 2021 for case 3. Please note that the model data shown only includes the Saharan dust while the lidar data shows also other aerosol particles and clouds. The profiles of backscatter coefficients measured by the lidar and predicted by the ICON-ART model for case C1 (averaged profiles from 13:30 to 14:30 for lidar measurements and profile at 14:00 for ICON-ART prediction on 19th, June 2021) and for case C2 (averaged profiles from 22:30 to 23:30 for lidar measurements and profile at 23:00 for ICON-ART prediction on 19th, June 2021) are shown on the right side of this figure. The vertical dashed lines in the contour plots indicate dust arrival (T1), dust touched to the ground (T2 & T4), and dust particle removal due to precipitation (T3 & T5). C1 and C2 represent time periods used for a more detailed data analysis as shown in the right side of this figure.

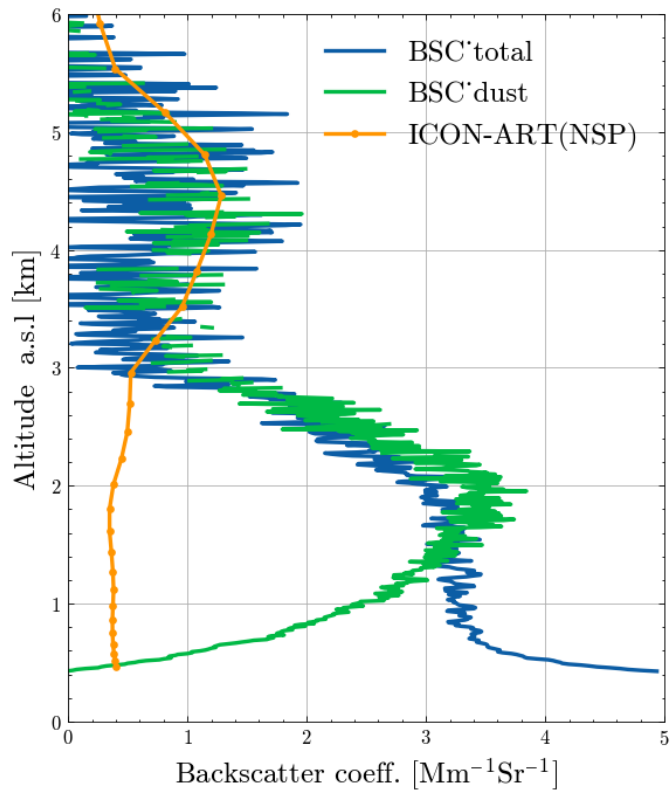


Figure 7. Vertical profile of total backscatter coefficients and dust backscatter coefficients from KASCAL and the predicted backscatter coefficient for non-spherical (NSP) particles from ICON-ART for period C3 (averaged profiles from 22:30 to 23:30 for lidar measurements and profile at 21:00 for ICON-ART prediction on 19th, June 2021) as indicated in Figure 6.

This plot shows a dust plume arrival at Rottenburg at 11:00 (± 20 min) on 19th, June 2021 with an initial dust layer height between 4.0 - 5.0 km and lasting for nearly two days. Since 23:30 on 19th, June 2021, a relative thick dust layer between ground level and up to 6.0 km was over Rottenburg. The dust layer heights and their peak heights for both lidar measurements and ICON-ART predictions for this Saharan dust case are shown in Figure 10c. The dust peak heights from KASCAL after 02:00, 20th, June 2021 are not shown in this panel as low clouds and precipitation impeded the retrieval of dust peak heights from lidar measurement. This figure shows that the dust layer heights from ICON-ART predictions and lidar measurements show similar trends but still show some discrepancies. The ICON-ART predicted dust layer heights are 900 ± 693 m higher than those retrieved from lidar measurements between 13:00 on June 19th and 02:00 on June 20th, 2021. The time series of particulate mass concentrations (PM_{2.5} and PM₁₀) from Fidas measurements and dust mass concentration from the ICON-ART simulation, shown in Figure 6f, do not a good correlation, with a slope of 0.56 ± 0.106 and a Pearson correlation coefficient of 0.383. This discrepancy may be caused by the model sample location is different from measurement location with distance of 40 km. The vertical profiles of the backscatter coefficients from lidar retrievals and ICON-ART predictions for two selected



periods indicated as C1 and C2 in Figure 6 are shown on the right side of Figure 6. For case C1, the backscatter coefficients
320 predicted by ICON-ART for non-spherical particles is systematically lower than those retrieved from lidar measurements by a factor of 3.91 ± 1.66 between 2.6 - 4.4 km. There are two possible reasons for this underestimation of the backscatter coefficients. One is that ICON-ART underestimated the dust loading in this case and the second explanation is that the Saharan dust particles acted as ice-nucleating particles at this altitude, promoting the formation or growth of ice crystals, which increases the particle size and enhances the lidar backscatter. For period C2, the backscatter coefficients predicted by ICON-ART were
325 lower by a factor of 7.48 ± 1.9 below 3.2 km. The first reason for this difference of the backscatter coefficients is because of the additional presence of non-dust particles which are not included in this specific model calculation. So we separated the backscatter coefficients into the dust part and non-dust part as was done also for Saharan dust case 2. The results are shown in Figure 7, which shows that the presence of non-dust particles cannot explain the complete difference as the pure dust backscatter coefficients are still higher than those calculated by ICON-ART. The second possible reason for this remaining
330 difference is that ICON-ART may underestimate the dust loading in the lower layer in this case. Although the ICON-ART results doesn't seem to agree with lidar measurements for this lower altitude, some consistency between model simulations and lidar measurement can also be seen for the dust layer above. The dust layer between 3.2 - 6.0 km for period C2 is also shown on the right side of Figure 6 with a good agreement between model simulation and lidar measurement.

3.4 Case 4

335 The Saharan dust case 4 was measured at the KIT campus north from 16th, March 2022 to 21th, March 2022. This Saharan dust plume was the most dense dust outbreak among all 4 cases with an AOD reaching values of 1.8 ± 0.07 at a wavelength of 550 nm in Karlsruhe. Figure S4 shows the horizontal distribution of daily averaged aerosol optical depth (AOD) from MODIS satellite observations at a spatial resolution of $0.4^\circ \times 0.4^\circ$, for the period of March 16–21, 2021. During this time, Saharan dust originating in North Africa was transported toward Karlsruhe, Germany. The MODIS retrieval clearly depicts the
340 presence of atmospheric dust plumes, exhibiting notably consistent spatial patterns. In particular, high AOD values over North Africa and the Middle East correspond well with established dust source regions. Figure 8 shows the time series of RCS for the polarized channel, cross-polarized channel, and LVDR from KASCAL measurements. The backscatter coefficients and particle depolarizations are not shown in this figure since their retrieval was impeded due to the presence of clouds from time to time. Figure 8 also shows the time series of ICON-ART predicted backscatter coefficients, particle number distributions, particulate
345 matter concentrations, and ground level meteorological parameters (e.g. wind, precipitation, WS700). The KASCAL conducted two-angle fixed pointed measurements during this field campaign in a similar way as for Saharan dust cases 1 and 2. As can be seen from this figure, the Saharan dust arrived in Karlsruhe at 12:00 on 16th, March 2022 at an altitude between 2.0-3.5 km, and a cloud began to appear at 00:00 on 17th, March 2022 at an altitude above 2.0 km. From 12:00 of 17th March to 12:00 of 18th March 2022, the presence of low level clouds and intermittent drizzle prevented the observation of the dust plume by KASCAL. On midday of 18th, March 2022, another dust plume arrived in Karlsruhe at an altitude of 2.0 - 3.0 km and subsequently sunk to lower altitudes. This latter dust plume was less intensive than that observed on 16th March 2022 as can be seen from the lower LVDR shown in panel (b) of this figure. The large particles observed at the surface by the Fidas

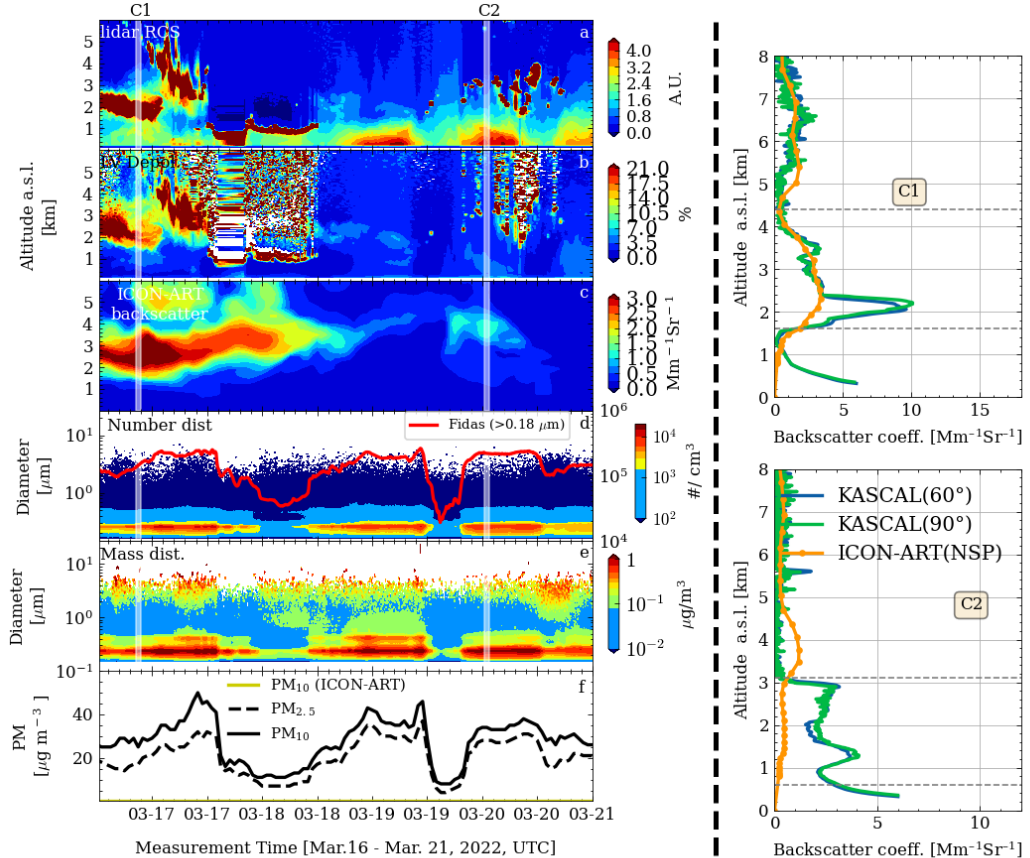


Figure 8. Time series of range corrected lidar signal for cross-polarized channel (a), and Linear Volume Depolarization Ratio (LVDR) (b) from KASCAL measurements, backscatter coefficients predicted by ICON-ART (c), particle number concentration (d), particle mass size distribution from Fidas 200 (e), and particulate matter concentrations PM_{2.5} & PM₁₀ from the Fidas 200 and the lowest model level (150 m) of the ICON-ART simulation (f) from March 16th to 21th, 2022 for case 4. Please note that the model data shown only includes the Saharan dust while the lidar data shows also other aerosol particles and clouds. The profiles of backscatter coefficients measured by the two lidars and predicted by ICON-ART model for C1 case (Averaged profiles from 20:30 to 21:30 for lidar measurement and profile at 21:00 for ICON-ART prediction on 16th, March 2022) and for C2 case (Averaged profiles from 00:30 to 01:30 for lidar measurement and profile at 01:00 for ICON-ART prediction on 20th, March 2022) are shown on the right side of this figure. C1 and C2 represent time periods used for a more detailed data analysis as shown in the right side of this figure.



200 were not reproduced by the ICON-ART model, as shown in Figure 8f. In addition, two special periods (C1 and C2) are highlighted in this figure. These periods were used to further investigate dust properties measured by lidar and predicted by the
 355 ICON-ART model for different dust mass loadings.

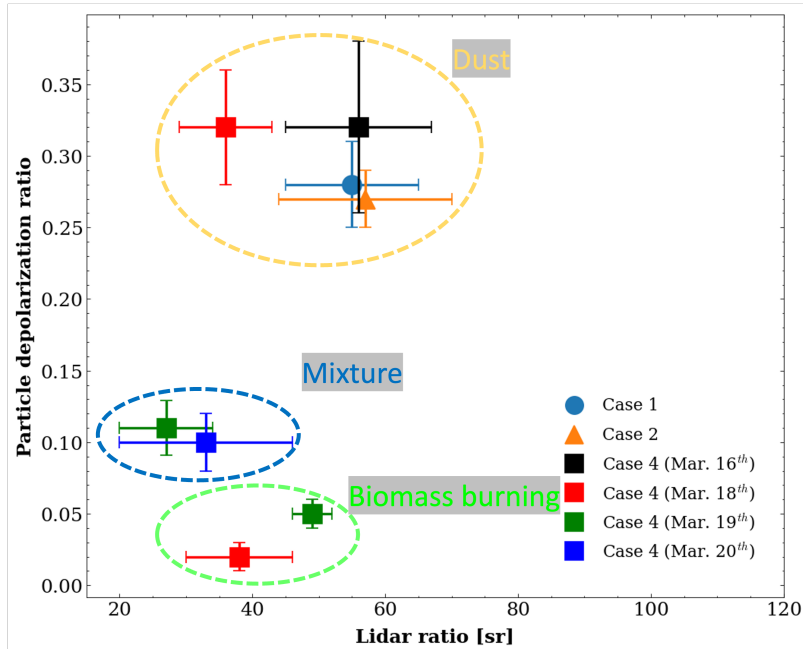


Figure 9. Linear Particle Depolarization Ratio (LPDR) versus lidar ratio retrieved from KASCAL for aerosol layers observed on different days across three Saharan dust cases. The lidar ratio for Case 3 is not available due to the absence of reliable lidar measurements during cloud-free nighttime periods.

Figure 9 presents the Linear Particle Depolarization Ratio (LPDR) versus lidar ratio retrieved from KASCAL for aerosol layers observed on different days for Saharan dust cases 1,2, and 4. The lidar ratio for Case 3 is not included due to the lack of reliable lidar data during cloud-free nighttime periods. For Cases 1 and 2, depolarization ratios of 0.28 ± 0.03 and 0.27 ± 0.02 , and lidar
 360 ratios of 55 ± 10 and 57 ± 13 , respectively, were retrieved—values that are consistent with previous studies (Freudenthaler et al., 2009; Schuster et al., 2012; Cao et al., 2014). Case 4 reveals the presence of Saharan dust, biomass burning aerosols, and their mixtures. On March 16, 2022, a dense dust layer was observed, characterized by a high depolarization ratio (0.32 ± 0.06) and a lidar ratio of 56 ± 11 . On March 18, two distinct layers were identified: an upper dust layer (LPDR: 0.32 ± 0.04 , lidar ratio: 38 ± 8) and a lower biomass burning aerosol layer (LPDR: 0.02 ± 0.003 , lidar ratio: 36 ± 7). On March 19, a mixed layer of Saharan dust and biomass burning aerosols (LPDR: 0.11 ± 0.019 , lidar ratio: 27 ± 7) was observed below a pure biomass
 365 burning aerosol layer (LPDR: 0.05 ± 0.004 , lidar ratio: 49 ± 3). By March 20, the layers had mixed more uniformly, with LPDR and lidar ratio values of 0.1 ± 0.02 and 33 ± 13 , respectively. The temporal evolution of LPDR and lidar ratios throughout



Case 4 highlights the progressive mixing between Saharan dust and biomass burning particles, particularly black carbon-rich aerosols (BLA). Early in the event (e.g., March 16), the presence of a distinct dust layer with high LPDR and lidar ratio values 370 reflects the dominance of non-spherical, coarse-mode mineral particles. As the episode progresses (e.g., March 18–20), the observed decrease in LPDR and variation in lidar ratios indicate increasing influence from biomass burning aerosols, which are primarily composed of fine-mode, spherical particles with strong light-absorbing properties due to the presence of black carbon. This mixing results in intermediate depolarization values and variable lidar ratios, depending on the relative abundance of dust and BLA in the column. The vertical layering—such as biomass burning aerosols overlaying dust—further suggests 375 long-range transport of smoke from regions affected by biomass combustion. These findings underscore the complexity of aerosol interactions and their evolving optical properties during long-range transport events involving multiple sources.

The evolution of the dust plume over Karlsruhe for dust case 4 predicted by the ICON-ART model is shown in panel (d) of Figure 8. This plot shows that two dust plumes arrived at Karlsruhe during these six days. The first dust plume arrived at 380 Karlsruhe at 00:00 on 16th, March 2022 with an initial dust layer height between 2.0 - 4.0 km and lasted nearly 3 days. This dust plume was relatively dense until 00:00 on 18th, March 2022 and was washed out by precipitation on 00:00 on 18th, March 2022. Another less dense dust plume arrived at Karlsruhe at 06:00 on 21th, March 2022 at an altitude of 2.0-3.0 km. The dust layer heights and their peak heights for both lidar measurement and ICON-ART prediction for this Saharan dust case 385 are shown in Figure 10d. The dust layer heights from ICON-ART prediction and lidar measurement show good agreement with each other. The vertical profiles of the backscatter coefficient from lidar retrieval and ICON-ART prediction for two selected periods indicated as C1 and C2 in Figure 8 are shown on the right side of Figure 8. For case C1, the vertical profile 390 of backscatter coefficients predicted by ICON-ART for non-spherical particles agrees well with those retrieved from lidar measurements except for peak of backscatter coefficients at altitudes between 1.6 km and 2.4 km. One possible reason for this phenomenon is that the ICON-ART model cannot resolve this small scale vertical aerosol distributions. For case C2, the backscatter coefficients predicted by ICON-ART are significantly lower than those observed below 3.2 km. One reason for this difference is the contribution of non-dust particles. Another possible reason is that ICON-ART overestimates the washout 395 effect by precipitation in this case. Figure S5 shows that the contribution of non-dust aerosol particles cannot explain the complete difference as the pure dust backscatter coefficients are still higher by a factor of 5.41 ± 2.27 than those predicted by ICON-ART. Hence, further reasons for this difference should be investigated.

3.5 Dust modelling vs. observations for all cases

395 Table 2 summarizes the key optical parameters of Saharan dust retrieved from lidar and sun-photometer observations for all four investigated cases. As noted earlier, the lidar ratio for Case 3 is not reported because no reliable lidar signals were available during cloud-free nighttime periods, and the single-scattering albedo (SSA) for this case is also excluded due to persistent cloud contamination. Overall, the retrieved optical properties exhibit values that are consistent with well-established 400 characteristics of transported Saharan dust. In particular, the lidar ratios (LR), depolarization ratios, and SSA values fall within the range of previously reported measurements over North Africa and downwind regions (Freudenthaler et al., 2009; Schuster et al., 2012; Cao et al., 2014). This agreement suggests that our retrieval procedure accurately captures the microphysical



Table 2. Overview of optical parameters of Saharan dust determined from lidar data, sun photometer measurements, and ICON-ART simulations for all four Saharan dust cases.

Parameter	λ [nm]	Case 1	Case 2	Case 3	Case 4	Average	Reference
BSC. ($\text{Mm}^{-1}\text{sr}^{-1}$)	355	0.95 ± 0.23	0.91 ± 0.43	1.52 ± 0.31	3.17 ± 2.48	1.64 ± 0.70	this work (lidar)
BSC. ($\text{Mm}^{-1}\text{sr}^{-1}$)	355	0.71 ± 0.37	1.15 ± 0.41	0.73 ± 0.30	0.77 ± 0.73	0.84 ± 0.47	this work (ICON-ART) 0.252 ± 0.03
LPDR	355	0.28 ± 0.03	0.27 ± 0.02	0.31 ± 0.04	0.30 ± 0.03	0.29 ± 0.03	(Haarig et al. 2017)
LR (sr)	355	46 ± 10	57 ± 13		55 ± 10	53 ± 11	48 ± 8 (Haarig et al. 2022)
AOD	340	0.21 ± 0.12	0.33 ± 0.12	0.52 ± 0.14	0.80 ± 0.42	0.47 ± 0.20	this work (sun photometer)
AOD	500	0.25 ± 0.11	0.39 ± 0.12	0.57 ± 0.12	0.91 ± 0.42	0.53 ± 0.19	this work (sun photometer)
AOD	500	0.17 ± 0.09	0.36 ± 0.22	0.24 ± 0.10	0.18 ± 0.06	0.24 ± 0.12	this work (ICON-ART)
AOD	1020	0.30 ± 0.11	0.41 ± 0.14	0.69 ± 0.12	1.01 ± 0.43	0.60 ± 0.20	this work (sun photometer)
SSA	439	0.92 ± 0.03	0.90 ± 0.27		0.93 ± 0.01	0.91 ± 0.10	0.91 (Müller et al., 2011) 0.86 - 0.98
SSA	870	0.93 ± 0.04	0.95 ± 0.23		0.95 ± 0.01	0.94 ± 0.09	(Cachorro et.al., 2018)

BSC: backscatter coefficient; Exc: extinction coefficient; LR: lidar ratio; LPDR: linear particle depolarization ratio.

AOD: Aerosol optical depth, SSA: single scatter albedo

and radiative signatures of mineral dust. Taken together, the close agreement with established climatological values and the physically consistent variability across cases provide confidence in the robustness of our observational dataset and support its relevance for evaluating dust representations in radiative transfer models and numerical simulations.

405 Figure 10 shows the time series of dust base height, dust top height, and dust peak height for both lidar measurements and ICON-ART simulations. The plume boundaries were determined using the backscatter coefficient, applying a threshold of 1 Mm . This figure shows that the dust arrival times predicted by the ICON-ART model agrees well with lidar measurements (± 20 minutes) for all 4 cases. This plot also shows that the dust layer heights predicted by ICON-ART and measured by lidar show good agreements for most of the time. However, some inconsistencies are visible for certain time periods (e.g. the first half of

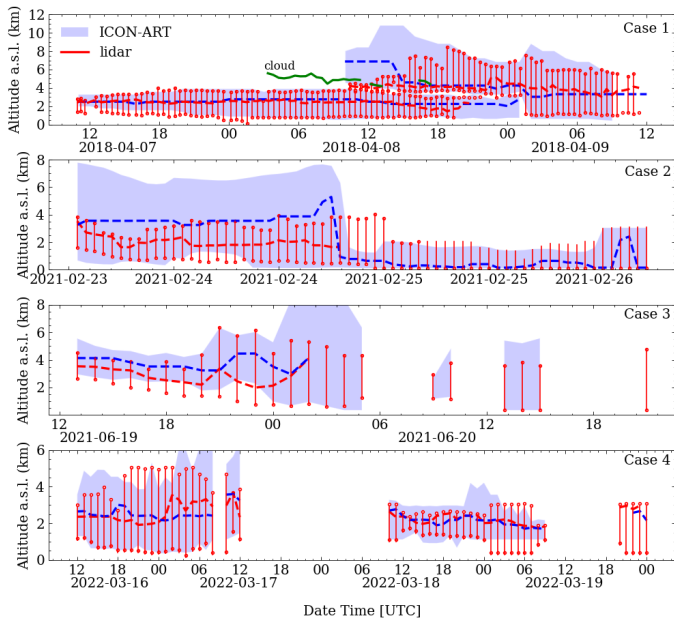


Figure 10. Time series of Saharan dust layer heights (vertical extend) and their peak heights (heights of maximum backscatter coefficients, indicated as red (lidar) and blue (ICON-ART) solid line) from both lidar measurements (red bars) and ICON-ART predictions (light blue area) for cases 1 - 4.

410 case 2 as shown in Figure 10b). The remaining discrepancies between observations and ICON-ART predictions may be related to the following reasons: 1) The ICON-ART model simulation used a relatively coarse horizontal resolution (20 km), which means that ICON-ART simulation results can't reflect structural details of Saharan dust plumes in such detail as possible e.g. by lidar measurements. Therefore, larger differences are to be expected especially for inhomogeneously structured dust plumes e.g. within thin filaments. In the future, this may be improved with higher-resolution ICON-ART calculations. 2) Depending 415 on the different meteorological conditions during transport of the dust plumes from Africa to Germany, especially the washout of dust particles may need improved parameterizations. This may be improved also using remote sensing technologies like lidar, satellite data, online data assimilation in model, etc.. 3). The inappropriate meteorological background information used in ICON-ART may also cause the discrepancy between model simulation and observation data.

420 Figure 11 shows the correlation of dust base heights, dust peak heights, and dust top heights from lidar measurements and ICON-ART predictions for the four Saharan dust cases. The blue-shaded area in these plots indicates slopes between 0.75 and 1.25 and the number shown in the left upper corner of each plot is the percentage of data points within this blue-shaded area. These plots show that there are 51%, 61%, and 61% of all data points within this blue-shaded area for dust base heights, dust peak heights, and dust top heights, respectively. To be clear, good agreement in dust layer heights can be seen for case 1, case 425 3, and case 4 but not for case 2 as discussed before. In general, the ICON-ART model predicts dust arrival times and dust layer

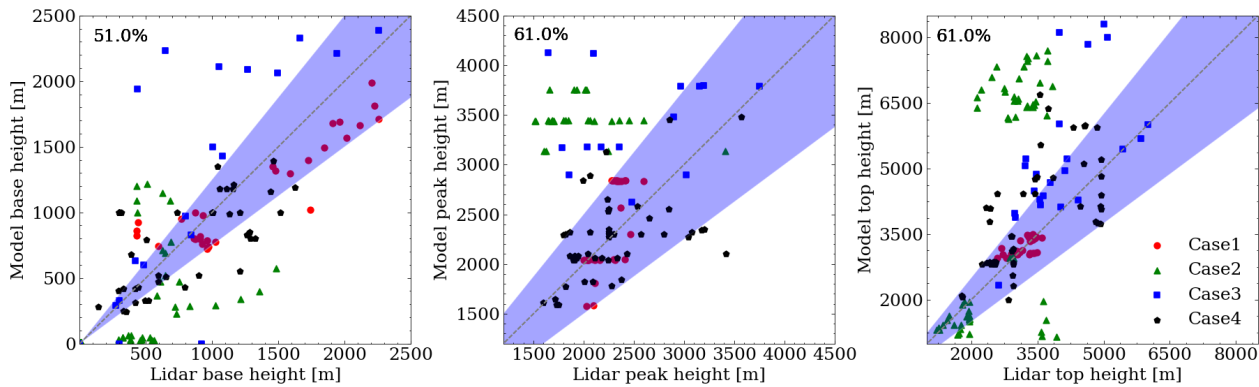


Figure 11. Correlation of dust base heights (left), dust peak heights (middle), and dust top heights (right) from lidar measurements and ICON-ART simulations for all 4 Saharan dust cases. The blue-shaded area indicates slopes between 0.75 and 1.25 and the number shown in the left upper corner is the percentage of data points within this blue-shaded area.

heights very well if considering the spatial resolution of the ICON-ART model (20.0 km horizontally).

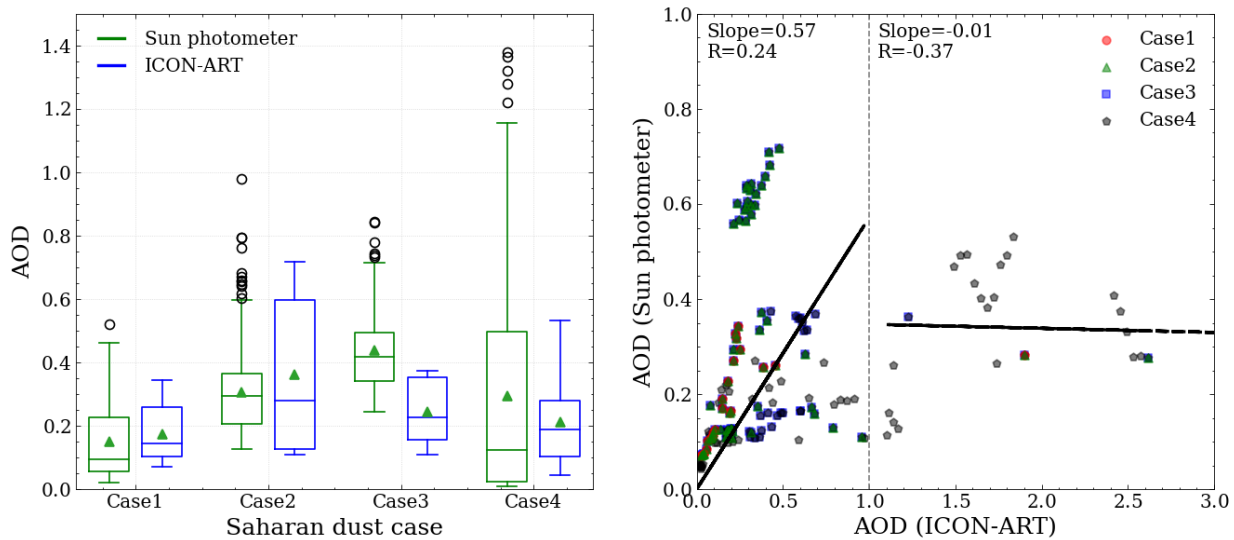


Figure 12. Distribution (left) and correlation (right) of coarse model aerosol optical depths (AODs) both from sun photometer measurement for total aerosol and ICON-ART predictions for Saharan dust only for all four Saharan dust cases at wavelength of 500 nm.

Figure 12 shows the distribution and correlation of coarse model AOD values at a wavelength of 500 nm from sun photometer measurements and ICON-ART predictions for all 4 Saharan dust cases. The boxplots display the interquartile range (box), median (horizontal line), and mean (filled triangle), with whiskers extending to 1.5 times the IQR and outliers shown as open



circles. Green and blue indicate the Sun-photometer observations and ICON-ART simulations, respectively. The AOD values given on the left side of this figure show that Saharan dust case 4 had the largest AOD with a value of 0.30 ± 0.39 , which indicates that the Saharan dust case 4 had the highest dust loading among these four cases. In addition, the AOD predicted by the ICON-ART model is systematically lower than the values measured by the sun photometer, except for Case 3, in which 435 the model partially overestimates AOD, possibly due to precipitation, as shown in Figure 6. This overestimation may indicate that ICON-ART underestimates the washout efficiency in its simulation, leading to an excess of Saharan dust particles. The correlation of the coarse-resolution model AOD values shown on the right side of the figure also indicates that ICON-ART systematically underestimates AOD. The AOD values exhibit a reasonable correlation, with a slope of 0.57 and a Pearson 440 correlation coefficient of 0.24 when AOD is less than 1.0. However, both the slope and the correlation coefficient become negative when AOD exceeds 1.0. Most of the data points with AOD greater than 1.0 correspond to Case 4, during which a strong haze event occurred over Karlsruhe as shown in Figure 8. This haze event was captured by the sun photometer but not represented in the ICON-ART model simulation. Overall, the ICON-ART model tends to underestimate AOD compared with sun photometer observations, except for Case 3, where precipitation may have led to an overestimation due to underestimated washout efficiency. The correlation analysis further confirms this systematic underestimation, with reasonable agreement (slope 445 = 0.57, $r = 0.24$) for $AOD < 1.0$, while negative correlations occur for $AOD > 1.0$, mainly influenced by the unmodeled strong haze event in Case 4.

3.6 Discussion of the consistency and discrepancies between observations and simulations

ICON-ART demonstrates skill in capturing the synoptic timing and vertical extent of major dust plumes. However, its coarse resolution limits the representation of small-scale mixing processes, and its simplified aerosol microphysics constrains the 450 variability of optical properties. The discrepancies between the model and observation are thus a result of four interconnected factors:

1- Unresolved turbulent and convective mixing processes: A primary factor is the model's horizontal resolution of 20 km. This coarse scale limits ICON-ART's ability to resolve small-scale turbulent eddies and local convective motions that are critical for vertical mixing. Consequently, the model struggles with boundary layer entrainment processes, where dust from the 455 free troposphere is incorporated into the growing mixed layer, and with plume-boundary layer interactions. The lidars directly observe the results of this mixing (sharp gradients and filamentary structures) which are parameterized rather than explicitly resolved in the model. These limitations are most pronounced in cases where plume-boundary layer interaction and aerosol mixing play a dominant role (e.g. case 4).

2- Simplifications in aerosol microphysical and optical properties: ICON-ART treats dust using a modal scheme with 460 prescribed particle size distributions and fixed optical properties assuming non-spherical particles. This approach constrains the natural variability of the aerosol population. In reality, dust microphysical properties such as size, shape, and composition evolve through processes during transport (e.g., aging and coating with other aerosol species). These processes modify the aerosol's hygroscopicity and single-scattering properties, directly impacting the backscatter coefficient.

3- Aerosol type mismatch: An important limitation arises from the different fundamental representations of aerosols in the



465 lidar observations and the ICON-ART simulations. The lidar backscatter coefficient is an observable that is sensitive to all aerosol types and mixtures present in the atmospheric column, including mineral dust, sea salt, biomass burning aerosols, and anthropogenic pollution. In contrast, the ICON-ART setup used here only represents mineral dust aerosols. Therefore, the observed backscatter values can be significantly higher than the modeled values, particularly in layers influenced by background aerosols or by co-transported species such as smoke or pollution that are not accounted for in the model.

470 **4- Assumptions of the Lidar measurements:** The lidar retrievals themselves are subject to assumptions, such as the use of a fixed lidar ratio (extinction-to-backscatter ratio) and calibration uncertainties, which can introduce biases in the absolute values of backscatter. While the relative vertical structures are robust, quantitative comparisons of backscatter magnitude must therefore be interpreted with caution.

475 **5- Improvement:** To mitigate these issues in future modeling studies, two pivotal advancements are recommended. First, employing convection-permitting resolutions (< 5 km) is essential to better resolve turbulent eddies and convective mixing, which would yield a more realistic representation of entrainment processes and plume-boundary-layer interactions. Second, transitioning to a more sophisticated aerosol scheme that explicitly represents processes like the formation of secondary organic aerosols and internal mixing (e.g., dust coating) would allow particle composition and size distributions to evolve dynamically, thereby significantly improving the simulation of aerosol optical properties and providing a more robust comparison with lidar 480 observations.

4 Conclusions

485 A comprehensive set of data was collected from remote sensing, in-situ measurements, and transport modelling to investigate Saharan dust transport, optical properties, and microphysical properties over Europe. This comprehensive dataset allowed characterization of Saharan dust plumes from multiple perspectives, providing a robust foundation for model validation and physical interpretation.

The comparison between lidar and sun photometer measurements proved effective in capturing key optical properties such as aerosol optical depth (AOD), which showed consistency with previous studies. Additionally, ICON-ART model simulations showed good agreement with observational data in terms of dust arrival time (± 20 minutes), dust layer heights (± 50 m), plume structure, and backscatter coefficients ($\pm 0.16 \text{ Mm}^{-1} \text{ sr}^{-1}$ at 355 nm), validating its predictive capability for Saharan dust events 490 over Western Europe. However, notable deviations were observed in certain periods, particularly regarding underestimated or overestimated dust loadings and discrepancies in vertical structure during complex meteorological conditions. These deviations highlight areas for model improvement, particularly in the representation of dust microphysical properties and removal processes. This study also highlights the significant role of wet removal in reducing atmospheric dust concentrations. In Case 3 and Case 4, a moderate rainfall event with an intensity of approximately 0.6 mm/h led to a substantial decrease in ground-level 495 dust concentrations, as observed in both in situ measurements and lidar profiles. This observation underscores the efficiency of even light precipitation in removing dust particles from the atmosphere and the necessity of accurately parameterizing wet deposition processes in dust transport models. The timing and magnitude of these reductions also suggest that wet scavenging



should be more explicitly represented, especially for events with persistent rainfall or drizzle that can effectively cleanse the boundary layer.

500 The systematic comparisons under different meteorological conditions and at various locations support model validation efforts and point toward future improvements in simulating dust emission, transport, aging, and removal mechanisms. Such enhancements are essential for better prediction of the climatic and air quality impacts of mineral dust across Europe.

Code availability. The code used to analyse the lidar data is property of Raymetics Inc, but we have shown that it generates the same results as the code single calculus chain (SCC) provided by EARLIENT https://www.earlinet.org/index.php?id=earlinet_homepage, last access: 8 505 March 2021). ICON-ART code are available upon request from the data originator (DWD; datenservice@dwd.de).

Data availability. The lidar raw data and in situ data are available via the open access data repository KIT open (doi will be added). Sun photometer data are available from the AErosol RObotic NETwork (Aeronet) data center at <https://aeronet.gsfc.nasa.gov/> (last access: 22 October 2025). ICON-ART model simulation results are available upon request from the data originator (DWD; datenservice@dwd.de).

510 *Author contributions.* FW, HS, and HZ performed the measurements. GAH, HV, and JF conducted the model simulations and post processing of the outputs. HZ and FW analysed the remote sensing data. HZ did write the manuscript with support from FW and HS as well as contributions from all co-authors.

Competing interests. At least one of the (co-)authors is a member of the editorial board of Atmospheric Chemistry and Physics.

Acknowledgements. Support by the staff of the Institute of Meteorology and Climate Research, and support by the project Modular Observation Solutions for Earth Systems (MOSES) of the Helmholtz Association (HGF).



515 References

Ansmann, A., Bösenberg, J., Chaikovsky, A., Comerón, A., Eckhardt, S., Eixmann, R., Freudenthaler, V., Ginoux, P., Komguem, L., Linné, H., Márquez, M. L., Matthias, V., Mattis, I., Mitev, V., Müller, D., Music, S., Nickovic, S., Pelon, J., Sauvage, L., Sobolewsky, P., Srivastava, M. K., Stohl, A., Torres, O., Vaughan, G., Wandinger, U., and Wiegner, M.: Long-range transport of Saharan dust to northern Europe: The 11–16 October 2001 outbreak observed with EARLINET, *Journal of Geophysical Research: Atmospheres*, 108, 520 <https://doi.org/10.1029/2003JD003757>, 2003.

Avdikos, G.: Powerful Raman Lidar systems for atmospheric analysis and high-energy physics experiments, *EPJ Web of Conferences*, 89, 04003, <https://doi.org/10.1051/epjconf/20158904003>, publisher: EDP Sciences, 2015.

Barnaba, F. and Gobbi, G. P.: Aerosol seasonal variability over the Mediterranean region and relative impact of maritime, continental and Saharan dust particles over the basin from MODIS data in the year 2001, *Atmospheric Chemistry and Physics*, 4, 2367–2391, 525 <https://doi.org/10.5194/acp-4-2367-2004>, publisher: Copernicus GmbH, 2004.

Benincasa, F.: Forecast comparison — WMO SDS-WAS, <https://sds-was.aemet.es/forecast-products/dust-forecasts/forecast-comparison>, 2023.

Cao, C., Zheng, S., and Singh, R. P.: Characteristics of aerosol optical properties and meteorological parameters during three major dust events (2005–2010) over Beijing, China, *Atmospheric Research*, 150, 129–142, <https://doi.org/10.1016/j.atmosres.2014.07.022>, 2014.

530 Chapman, E. G., Gustafson, W. I. J., Easter, R. C., Barnard, J. C., Ghan, S. J., Pekour, M. S., and Fast, J. D.: Coupling aerosol-cloud-radiative processes in the WRF-Chem model: Investigating the radiative impact of elevated point sources, *Atmospheric Chemistry and Physics*, 9, 945–964, <https://doi.org/10.5194/acp-9-945-2009>, publisher: Copernicus GmbH, 2009.

Chouza, F., Reitebuch, O., Benedetti, A., and Weinzierl, B.: Saharan dust long-range transport across the Atlantic studied by an airborne Doppler wind lidar and the MACC model, *Atmospheric Chemistry and Physics*, 16, 11 581–11 600, <https://doi.org/10.5194/acp-16-11581-2016>, publisher: Copernicus GmbH, 2016.

535 Conceição, R., Silva, H. G., Mirão, J., Gostein, M., Fialho, L., Narvarte, L., and Collares-Pereira, M.: Saharan dust transport to Europe and its impact on photovoltaic performance: A case study of soiling in Portugal, *Solar Energy*, 160, 94–102, <https://doi.org/10.1016/j.solener.2017.11.059>, 2018.

Diop, D., Niang, D. N., Drame, M. S., and Ba, A.: Dust Source, Vertical Profile and Climate Impact by RegCM3 Regional Climate Model over West Africa during 2006, *Atmospheric and Climate Sciences*, 10, 206–219, <https://doi.org/10.4236/acs.2020.102011>, number: 2 540 Publisher: Scientific Research Publishing, 2020.

Dubovik, O. and King, M. D.: A flexible inversion algorithm for retrieval of aerosol optical properties from Sun and sky radiance measurements, *Journal of Geophysical Research: Atmospheres*, 105, 20 673–20 696, <https://doi.org/10.1029/2000JD900282>, _eprint: <https://onlinelibrary.wiley.com/doi/pdf/10.1029/2000JD900282>, 2000.

545 Freudenthaler, V.: About the effects of polarising optics on lidar signals and the Δ 90 calibration, *Atmospheric Measurement Techniques*, 9, 4181–4255, <https://doi.org/10.5194/amt-9-4181-2016>, publisher: Copernicus GmbH, 2016.

Freudenthaler, V., Esselborn, M., Wiegner, M., Heese, B., Tesche, M., Ansmann, A., Müller, D., Althausen, D., Wirth, M., Fix, A., Ehret, G., Knippertz, P., Toledano, C., Gasteiger, J., Garhammer, M., and Seefeldner, M.: Depolarization ratio profiling at several wavelengths in pure Saharan dust during SAMUM 2006, *Tellus B*, 61, 165–179, <https://doi.org/10.1111/j.1600-0889.2008.00396.x>, _eprint: 550 <https://onlinelibrary.wiley.com/doi/pdf/10.1111/j.1600-0889.2008.00396.x>, 2009.



Gasteiger, J., Wiegner, M., Groß, S., Freudenthaler, V., Toledano, C., Tesche, M., and Kandler, K.: Modelling lidar-relevant optical properties of complex mineral dust aerosols, *Tellus B: Chemical and Physical Meteorology*, 63, 725–741, <https://doi.org/10.1111/j.1600-0889.2011.00559.x>, 2011.

Giles, D. M., Sinyuk, A., Sorokin, M. G., Schafer, J. S., Smirnov, A., Slutsker, I., Eck, T. F., Holben, B. N., Lewis, J. R., Campbell, J. R., Welton, E. J., Korkin, S. V., and Lyapustin, A. I.: Advancements in the Aerosol Robotic Network (AERONET) Version 3 database – automated near-real-time quality control algorithm with improved cloud screening for Sun photometer aerosol optical depth (AOD) measurements, *Atmospheric Measurement Techniques*, 12, 169–209, <https://doi.org/10.5194/amt-12-169-2019>, publisher: Copernicus GmbH, 2019.

555 Guerzoni, S. and Chester, R., eds.: *The Impact of Desert Dust Across the Mediterranean*, vol. 11 of *Environmental Science and Technology Library*, Springer Netherlands, Dordrecht, <https://doi.org/10.1007/978-94-017-3354-0>, 1996.

560 Hermes, K., Quinting, J., Grams, C. M., Hoose, C., and Hoshyaripour, G. A.: Impact of Saharan dust outbreaks on short-range weather forecast errors in Europe, *Quarterly Journal of the Royal Meteorological Society*, 150, 1704–1723, <https://doi.org/https://doi.org/10.1002/qj.4666>, 2024.

Holben, B. N., Eck, T. F., Slutsker, I., Tanré, D., Buis, J. P., Setzer, A., Vermote, E., Reagan, J. A., Kaufman, Y. J., Nakajima, T., Lavenu, F., Jankowiak, I., and Smirnov, A.: AERONET - A federated instrument network and data archive for aerosol characterization, *Remote Sensing of Environment*, 66, 1–16, [https://doi.org/10.1016/S0034-4257\(98\)00031-5](https://doi.org/10.1016/S0034-4257(98)00031-5), 1998.

565 Hoshyaripour, G. A., Bachmann, V., Förstner, J., Steiner, A., Vogel, H., Wagner, F., Walter, C., and Vogel, B.: Effects of Particle Nonsphericity on Dust Optical Properties in a Forecast System: Implications for Model-Observation Comparison, *Journal of Geophysical Research: Atmospheres*, 124, 7164–7178, <https://doi.org/10.1029/2018JD030228>, _eprint: <https://onlinelibrary.wiley.com/doi/pdf/10.1029/2018JD030228>, 2019.

570 Jiang, F., Saathoff, H., Ezenobi, U., Song, J., Zhang, H., Gao, L., and Leisner, T.: Measurement report: Brown carbon aerosol in rural Germany – sources, chemistry, and diurnal variations, *Atmospheric Chemistry and Physics*, 25, 1917–1930, <https://doi.org/10.5194/acp-25-1917-2025>, 2025.

Justice, C., Townshend, J., Vermote, E., Masuoka, E., Wolfe, R., Saleous, N., Roy, D., and Morisette, J.: An overview of MODIS Land data processing and product status, *Remote Sensing of Environment*, 83, 3–15, [https://doi.org/10.1016/S0034-4257\(02\)00084-6](https://doi.org/10.1016/S0034-4257(02)00084-6), the Moderate Resolution Imaging Spectroradiometer (MODIS): a new generation of Land Surface Monitoring, 2002.

575 Jöckel, P., Tost, H., Pozzer, A., Brühl, C., Buchholz, J., Ganzeveld, L., Hoor, P., Kerkweg, A., Lawrence, M. G., Sander, R., Steil, B., Stiller, G., Tanarhte, M., Taraborrelli, D., van Aardenne, J., and Lelieveld, J.: The atmospheric chemistry general circulation model ECHAM5/MESSy1: consistent simulation of ozone from the surface to the mesosphere, *Atmospheric Chemistry and Physics*, 6, 5067–5104, <https://doi.org/10.5194/acp-6-5067-2006>, publisher: Copernicus GmbH, 2006.

580 Jöckel, P., Kerkweg, A., Pozzer, A., Sander, R., Tost, H., Riede, H., Baumgaertner, A., Gromov, S., and Kern, B.: Development cycle 2 of the Modular Earth Submodel System (MESSy2), *Geoscientific Model Development*, 3, 717–752, <https://doi.org/10.5194/gmd-3-717-2010>, publisher: Copernicus GmbH, 2010.

Kandler, K., Benker, N., Bundke, U., Cuevas, E., Ebert, M., Knippertz, P., Rodríguez, S., Schütz, L., and Weinbruch, S.: Chemical composition and complex refractive index of Saharan Mineral Dust at Izaña, Tenerife (Spain) derived by electron microscopy, *Atmospheric Environment*, 41, 8058–8074, <https://doi.org/10.1016/j.atmosenv.2007.06.047>, 2007.

585 Kim, D., Chin, M., Yu, H., Eck, T. F., Sinyuk, A., Smirnov, A., and Holben, B. N.: Dust optical properties over North Africa and Arabian Peninsula derived from the AERONET dataset, *Atmospheric Chemistry and Physics*, 11, 10 733–10 741, <https://doi.org/10.5194/acp-11-10733-2011>, publisher: Copernicus GmbH, 2011.



590 Kunz, A., Pan, L. L., Konopka, P., Kinnison, D. E., and Tilmes, S.: Chemical and dynamical discontinuity at the extratropical tropopause based on START08 and WACCM analyses, *Journal of Geophysical Research: Atmospheres*, 116, <https://doi.org/10.1029/2011JD016686>, _eprint: <https://onlinelibrary.wiley.com/doi/pdf/10.1029/2011JD016686>, 2011.

595 Kunz, M., Abbas, S. S., Bauckholt, M., Böhmländer, A., Feuerle, T., Gasch, P., Glaser, C., Groß, J., Hajnsek, I., Handwerker, J., Hase, F., Khordakova, D., Knippertz, P., Kohler, M., Lange, D., Latt, M., Laube, J., Martin, L., Mauder, M., Möhler, O., Mohr, S., Reitter, R. W., Rettenmeier, A., Rolf, C., Saathoff, H., Schrönn, M., Schütze, C., Spahr, S., Späth, F., Vogel, F., Völksch, I., Weber, U., Wieser, A., Wilhelm, J., Zhang, H., and Dietrich, P.: Swabian MOSES 2021: An interdisciplinary field campaign for investigating convective storms and their event chains, *Frontiers in Earth Science*, Volume 10 - 2022, <https://doi.org/10.3389/feart.2022.999593>, 2022a.

600 Kunz, M., Abbas, S. S., Bauckholt, M., Böhmländer, A., Feuerle, T., Gasch, P., Glaser, C., Groß, J., Hajnsek, I., Handwerker, J., Hase, F., Khordakova, D., Knippertz, P., Kohler, M., Lange, D., Latt, M., Laube, J., Martin, L., Mauder, M., Möhler, O., Mohr, S., Reitter, R. W., Rettenmeier, A., Rolf, C., Saathoff, H., Schrönn, M., Schütze, C., Spahr, S., Späth, F., Vogel, F., Völksch, I., Weber, U., Wieser, A., Wilhelm, J., Zhang, H., and Dietrich, P.: Swabian MOSES 2021: An interdisciplinary field campaign for investigating convective storms and their event chains, *Frontiers in Earth Science*, 10, <https://www.frontiersin.org/articles/10.3389/feart.2022.999593>, 2022b.

605 Liu, Z., Omar, A., Vaughan, M., Hair, J., Kittaka, C., Hu, Y., Powell, K., Trepte, C., Winker, D., Hostetler, C., Ferrare, R., and Pierce, R.: CALIPSO lidar observations of the optical properties of Saharan dust: A case study of long-range transport, *Journal of Geophysical Research: Atmospheres*, 113, <https://doi.org/10.1029/2007JD008878>, _eprint: <https://onlinelibrary.wiley.com/doi/pdf/10.1029/2007JD008878>, 2008.

Mallet, M., Tulet, P., Serça, D., Solmon, F., Dubovik, O., Pelon, J., Pont, V., and Thouron, O.: Impact of dust aerosols on the radiative budget, surface heat fluxes, heating rate profiles and convective activity over West Africa during March 2006, *Atmospheric Chemistry and Physics*, 9, 7143–7160, <https://doi.org/10.5194/acp-9-7143-2009>, publisher: Copernicus GmbH, 2009.

610 Merdji, A. B., Lu, C., Xu, X., and Mhawish, A.: Long-term three-dimensional distribution and transport of Saharan dust: Observation from CALIPSO, MODIS, and reanalysis data, *Atmospheric Research*, 286, 106 658, <https://doi.org/10.1016/j.atmosres.2023.106658>, 2023.

Middleton, N. J. and Goudie, A. S.: Saharan dust: sources and trajectories, *Transactions of the Institute of British Geographers*, 26, 165–181, <https://doi.org/10.1111/1475-5661.00013>, _eprint: <https://onlinelibrary.wiley.com/doi/pdf/10.1111/1475-5661.00013>, 2001.

615 Misra, A., Tripathi, S. N., Kaul, D. S., and Welton, E. J.: Study of MPLNET-Derived Aerosol Climatology over Kanpur, India, and Validation of CALIPSO Level 2 Version 3 Backscatter and Extinction Products, *Journal of Atmospheric and Oceanic Technology*, 29, 1285–1294, <https://doi.org/10.1175/JTECH-D-11-00162.1>, publisher: American Meteorological Society Section: *Journal of Atmospheric and Oceanic Technology*, 2012.

Molinaroli, E., Guerzoni, S., and Rampazzo, G.: Contribution of Saharan dust to the Central Mediterranean Basin, in: *Processes Controlling the Composition of Clastic Sediments*, edited by Johnsson, M. J. and Basu, A., vol. 284, p. 0, Geological Society of America, <https://doi.org/10.1130/SPE284-p303>, 1993.

620 Mona, L., Papagiannopoulos, N., Basart, S., Baldasano, J., Binietoglou, I., Cornacchia, C., and Pappalardo, G.: EARLINET dust observations vs. BSC-DREAM8b modeled profiles: 12-year-long systematic comparison at Potenza, Italy, *Atmospheric Chemistry and Physics*, 14, 8781–8793, <https://doi.org/10.5194/acp-14-8781-2014>, publisher: Copernicus GmbH, 2014.

Müller, D., Weinzierl, B., Petzold, A., Kandler, K., Ansmann, A., Müller, T., Tesche, M., Freudenthaler, V., Esselborn, M., Heese, B., Althausen, D., Schladitz, A., Otto, S., and Knippertz, P.: Mineral dust observed with AERONET Sun photometer, Raman lidar, and 625 in situ instruments during SAMUM 2006: Shape-independent particle properties, *Journal of Geophysical Research: Atmospheres*, 115, <https://doi.org/10.1029/2009JD012520>, _eprint: <https://onlinelibrary.wiley.com/doi/pdf/10.1029/2009JD012520>, 2010.



Pozzoli, L., Bey, I., Rast, S., Schultz, M. G., Stier, P., and Feichter, J.: Trace gas and aerosol interactions in the fully coupled model of aerosol-chemistry-climate ECHAM5-HAMMOZ: 1. Model description and insights from the spring 2001 TRACE-P experiment, *Journal of Geophysical Research: Atmospheres*, 113, <https://doi.org/10.1029/2007JD009007>, _eprint: 630 <https://onlinelibrary.wiley.com/doi/pdf/10.1029/2007JD009007>, 2008a.

Pozzoli, L., Bey, I., Rast, S., Schultz, M. G., Stier, P., and Feichter, J.: Trace gas and aerosol interactions in the fully coupled model of aerosol-chemistry-climate ECHAM5-HAMMOZ: 2. Impact of heterogeneous chemistry on the global aerosol distributions, *Journal of Geophysical Research: Atmospheres*, 113, <https://doi.org/10.1029/2007JD009008>, _eprint: 635 <https://onlinelibrary.wiley.com/doi/pdf/10.1029/2007JD009008>, 2008b.

Remer, L. A., Kaufman, Y. J., Tanré, D., Mattoe, S., Chu, D. A., Martins, J. V., Li, R.-R., Ichoku, C., Levy, R. C., Kleidman, R. G., Eck, T. F., Vermote, E., and Holben, B. N.: The MODIS Aerosol Algorithm, Products, and Validation, *Journal of the Atmospheric Sciences*, 62, 947 – 973, <https://doi.org/10.1175/JAS3385.1>, 2005.

Rieger, D., Bangert, M., Bischoff-Gauss, I., Förstner, J., Lundgren, K., Reinert, D., Schröter, J., Vogel, H., Zängl, G., Ruhnke, R., and 640 Vogel, B.: ICON-ART 1.0 – a new online-coupled model system from the global to regional scale, *Geoscientific Model Development*, 8, 1659–1676, <https://doi.org/10.5194/gmd-8-1659-2015>, 2015.

Rieger, D., Steiner, A., Bachmann, V., Gasch, P., Förstner, J., Deetz, K., Vogel, B., and Vogel, H.: Impact of the 4 April 2014 Saharan dust outbreak on the photovoltaic power generation in Germany, *Atmospheric Chemistry and Physics*, 17, 13 391–13 415, 645 <https://doi.org/10.5194/acp-17-13391-2017>, 2017a.

Rieger, D., Steiner, A., Bachmann, V., Gasch, P., Förstner, J., Deetz, K., Vogel, B., and Vogel, H.: Impact of the 4 April 2014 Saharan dust outbreak on the photovoltaic power generation in Germany, *Atmospheric Chemistry and Physics*, 17, 13 391–13 415, 650 <https://doi.org/10.5194/acp-17-13391-2017>, publisher: Copernicus GmbH, 2017b.

Roeckner, E., Brokopf, R., Esch, M., Giorgetta, M., Hagemann, S., Kornblueh, L., Manzini, E., Schlese, U., and Schulzweida, U.: Sensitivity of Simulated Climate to Horizontal and Vertical Resolution in the ECHAM5 Atmosphere Model, *Journal of Climate*, 19, 3771–3791, 655 <https://doi.org/10.1175/JCLI3824.1>, publisher: American Meteorological Society Section: *Journal of Climate*, 2006.

Rostási, , Topa, B. A., Gresina, F., Weiszburg, T. G., Gelencsér, A., and Varga, G.: Saharan Dust Deposition in Central Europe in 2016—A 660 Representative Year of the Increased North African Dust Removal Over the Last Decade, *Frontiers in Earth Science*, 10, <https://www.frontiersin.org/articles/10.3389/feart.2022.869902>, 2022.

Saidou Chaibou, A. A., Ma, X., and Sha, T.: Dust radiative forcing and its impact on surface energy budget over West Africa, *Scientific Reports*, 10, 12 236, <https://doi.org/10.1038/s41598-020-69223-4>, number: 1 Publisher: Nature Publishing Group, 2020.

665 Salomonson, V. V., Barnes, W., Maymon, P. W., Montgomery, H. E., and Ostrow, H.: MODIS: Advanced facility instrument for studies of the Earth as a system, *IEEE Transactions on geoscience and remote sensing*, 27, 145–153, <https://doi.org/10.1109/36.20292>, 1989.

Schuster, G. L., Vaughan, M., MacDonnell, D., Su, W., Winker, D., Dubovik, O., Lapyonok, T., and Trepte, C.: Comparison of CALIPSO aerosol optical depth retrievals to AERONET measurements, and a climatology for the lidar ratio of dust, *Atmospheric Chemistry and Physics*, 12, 7431–7452, <https://doi.org/10.5194/acp-12-7431-2012>, publisher: Copernicus GmbH, 2012.

670 Seifert, A., Bachmann, V., Filipitsch, F., Förstner, J., Grams, C. M., Hoshayaripour, G. A., Quinting, J., Rohde, A., Vogel, H., Wagner, A., and Vogel, B.: Aerosol–cloud–radiation interaction during Saharan dust episodes: the dusty cirrus puzzle, *Atmospheric Chemistry and Physics*, 23, 6409–6430, <https://doi.org/10.5194/acp-23-6409-2023>, 2023.



Sinyuk, A., Holben, B. N., Eck, T. F., Giles, D. M., Slutsker, I., Korkin, S., Schafer, J. S., Smirnov, A., Sorokin, M., and Lyapustin, A.: The AERONET Version 3 aerosol retrieval algorithm, associated uncertainties and comparisons to Version 2, *Atmospheric Measurement Techniques*, 13, 3375–3411, <https://doi.org/10.5194/amt-13-3375-2020>, publisher: Copernicus GmbH, 2020.

665 Smith, K., Garcia, R., Marsh, D., and Richter, H.: WACCM simulations of the mean circulation and trace species transport in the winter mesosphere, *Journal of Geophysical Research-Atmospheres*, <https://doi.org/10.1029/2011JD016083>, 2011.

Song, Q., Zhang, Z., Yu, H., Kok, J. F., Di Biagio, C., Albani, S., Zheng, J., and Ding, J.: Size-resolved dust direct radiative effect efficiency derived from satellite observations, *Atmospheric Chemistry and Physics*, 22, 13 115–13 135, <https://doi.org/10.5194/acp-22-13115-2022>, publisher: Copernicus GmbH, 2022.

670 Sugimoto, N., Nishizawa, T., Shimizu, A., and Jin, Y.: The Asian Dust and Aerosol Lidar Observation Network (AD-Net), in: *Light, Energy and the Environment* (2016), paper EW2A.1, p. EW2A.1, Optica Publishing Group, <https://doi.org/10.1364/EE.2016.EW2A.1>, 2016.

Tanaka, T. Y., Kurosaki, Y., Chiba, M., Matsumura, T., Nagai, T., Yamazaki, A., Uchiyama, A., Tsunematsu, N., and Kai, K.: Possible transcontinental dust transport from North Africa and the Middle East to East Asia, *Atmospheric Environment*, 39, 3901–3909,

675 <https://doi.org/10.1016/j.atmosenv.2005.03.034>, 2005.

Tesche, M., Ansmann, A., Müller, D., Althausen, D., Engelmann, R., Freudenthaler, V., and Groß, S.: Vertically resolved separation of dust and smoke over Cape Verde using multiwavelength Raman and polarization lidars during Saharan Mineral Dust Experiment 2008, *Journal of Geophysical Research: Atmospheres*, 114, <https://doi.org/10.1029/2009JD011862>, _eprint: <https://onlinelibrary.wiley.com/doi/pdf/10.1029/2009JD011862>, 2009.

680 Varga, G.: Changing nature of Saharan dust deposition in the Carpathian Basin (Central Europe): 40 years of identified North African dust events (1979–2018), *Environment International*, 139, 105 712, <https://doi.org/10.1016/j.envint.2020.105712>, 2020.

Vermeulen, A., Devaux, C., and Herman, M.: Retrieval of the scattering and microphysical properties of aerosols from ground-based optical measurements including polarization. I. Method, *Applied Optics*, 39, 6207–6220, <https://doi.org/10.1364/AO.39.006207>, publisher: Optica Publishing Group, 2000.

685 Vogel, B., Hoose, C., Vogel, H., and Kottmeier, C.: A model of dust transport applied to the Dead Sea Area, *Meteorologische Zeitschrift*, pp. 611–624, <https://doi.org/10.1127/0941-2948/2006/0168>, publisher: Schweizerbart'sche Verlagsbuchhandlung, 2006.

Vogel, H., Förstner, J., Vogel, B., Hanisch, T., Mühr, B., Schättler, U., and Schad, T.: Time-lagged ensemble simulations of the dispersion of the Eyjafjallajökull plume over Europe with COSMO-ART, *Atmospheric Chemistry and Physics*, 14, 7837–7845, <https://doi.org/10.5194/acp-14-7837-2014>, publisher: Copernicus GmbH, 2014.

690 Weimer, M., Schröter, J., Eckstein, J., Deetz, K., Neumaier, M., Fischbeck, G., Hu, L., Millet, D. B., Rieger, D., Vogel, H., Vogel, B., Reddmann, T., Kirner, O., Ruhnke, R., and Braesicke, P.: An emission module for ICON-ART 2.0: implementation and simulations of acetone, *Geoscientific Model Development*, 10, 2471–2494, <https://doi.org/10.5194/gmd-10-2471-2017>, publisher: Copernicus GmbH, 2017.

695 Wu, M., Liu, X., Yu, H., Wang, H., Shi, Y., Yang, K., Darmenov, A., Wu, C., Wang, Z., Luo, T., Feng, Y., and Ke, Z.: Understanding processes that control dust spatial distributions with global climate models and satellite observations, *Atmospheric Chemistry and Physics*, 20, 13 835–13 855, <https://doi.org/10.5194/acp-20-13835-2020>, publisher: Copernicus GmbH, 2020.

Zhang, H., Wagner, F., Saathoff, H., Vogel, H., Hoshayaripour, G., Bachmann, V., Förstner, J., and Leisner, T.: Comparison of Scanning LiDAR with Other Remote Sensing Measurements and Transport Model Predictions for a Saharan Dust Case, *Remote Sensing*, 14, 1693, <https://doi.org/10.3390/rs14071693>, number: 7 Publisher: Multidisciplinary Digital Publishing Institute, 2022.



700 Zängl, G., Reinert, D., Rípodas, P., and Baldauf, M.: The ICON (ICOahedral Non-hydrostatic) modelling framework of DWD and MPI-M: Description of the non-hydrostatic dynamical core, *Quarterly Journal of the Royal Meteorological Society*, 141, 563–579, <https://doi.org/10.1002/qj.2378>, _eprint: <https://onlinelibrary.wiley.com/doi/pdf/10.1002/qj.2378>, 2015.